University of New Mexico
UNM Digital Repository

Fall 12-17-2016

Drag and Shape Analysis of Fiberglass Particles

Cody Williams

Follow this and additional works at: https://digitalrepository.unm.edu/me_etds

Part of the Mechanical Engineering Commons

Recommended Citation

Cody Williams

_____
Candidate

Mechanical Engineering

_____
Department

This thesis is approved, and it is acceptable in quality and form for publication:

Approved by the Thesis Committee:

Yu-Lin Shen, Chairperson

_____

Edward Blandford

_____

Kerry Howe

_____

Arsalan Razani

_____

Drag and Shape Analysis of Fiberglass Particles

BY

Cody Williams

B.S., Mechanical Engineering, University of New Mexico, 2014

THESIS

Submitted in Partial Fulfillment of the
Requirements for the Degree of

Master of Science

Mechanical Engineering

The University of New Mexico
Albuquerque, New Mexico

December, 2016

Drag and Shape Analysis of Fiberglass Particles

by

Cody Williams

B.S., Mechanical Engineering, University of New Mexico, 2014

Abstract

Settling tests were performed on particles of NUKON fiberglass to relate the drag coefficient of the particles to the Reynolds number of the particles. A new method was developed to measure fiberglass particles. The projected area, projected perimeter, and average height of the particles are measured using this method. The measurements are used to calculate the measured drag coefficient and measured Reynolds number for the particles. Data collected was compared to previous studies that focused on the settling of sand grains. A predictive correlation that was developed for sand grains was applied towards the particles of fiberglass. Tests were run with dyed particles of fiberglass as a means of flow visualization. The results from these visualization tests were compared with results from the free settling of disks.

Contents

List of Figures

List of Abbreviations

BWR	Boiling Water Reactor
CSF	Corey Shape Factor
ECCS	Emergency Core Cooling System
GL	Generic Letter
GSI	Generic Safety Letter
HELB	High Energy Line Break
LOCA	Loss of Coolant Accident
NEI	Nuclear Energy Institute
NRC	Nuclear Regulatory Commission
NUREG/CR	Nuclear Regulatory Commission Regulation Contractor Report
PWR	Pressurized Water Reactor
TAMU	Texas Agriculture and Mining University
UNM	University of New Mexico
ZOI	Zone of influence

List of Symbols

A	Projected area of a particle
A_*	Stokes flow coefficient in the Cheng correlation
a	Major axis of a particle
B	Drag limit coefficient in the Cheng correlation
b	Intermediate axis of a particle
C_D	Drag coefficient
c	Minor axis of a particle
F_B	Buoyant force
F_D	Drag force
F_g	Force due to gravity
g	Gravitational acceleration
h	Average height of a particle
L	Characteristic length of a particle
n	Empirical constant in the Cheng correlation
P	Projected perimeter of a particle, Roundness factor
ΔP	Pressure difference
Re	Reynolds number
r	Radius of an individual fiber
u	Terminal settling velocity of a particle
u_t	Velocity through a porous medium
V	Volume of a particle
κ	Permeability of a porous medium
μ	Dynamic viscosity of water
ν	Kinematic viscosity of water
ρ	Density of water
ρ_f	Density of NUKON fiberglass
ρ_p	Density of fiberglass particle
ϕ	As fabricated porosity of NUKON fiberglass
ϕ_*	Solid fraction of fiberglass particle

Chapter 1 Introduction

In 2004, the United States Nuclear Regulatory Commission (NRC) Identified Generic Safety Issue (GSI) 191 which involves the potential for blockage of the emergency core cooling system (ECCS) sump strainers by means of debris that is found inside containment [1]. The blockage can only occur during a loss of coolant accident (LOCA). During which one or more pressurized high energy coolant carrying lines break and subsequently discharges large amounts of piping insulation. The initial burst from the high energy line would shred this insulation into small pieces which are then collected on the floor, and ultimately transported via the water from the break towards the ECCS sump strainers. Once the debris is collected on the sump strainers there exists the possibility that the pressure drop across the strainer could increase enough to compromise ECCS performance.

The original driver for this safety issue is three well documented historical cases [1], all involving boiling water reactors (BWRs) where the potential for debris to compromise sump strainers was shown. The first instance occurred in 1992 at a Swedish BWR called Barsebäck Unit 2 where the accidental opening of a relief valve caused mineral wool insulation to be dispersed and transported along containment and collected on the strainer of the containment spray system, eventually causing a need to back wash the strainers. The second incident occurred at an NRC regulated plant in Ohio named Perry Unit 1 in 1993. This plant had two sump strainer blockage instances happen within the span of a year. The first incident at Barsebäck, the ECCS strainers were clogged with particulate matter and the second time at Perry the strainers were clogged with glass fibers from ventilation filters. In both cases, the blocking of the strainers induced head loss so high that the strainers were deformed. The third incident occurred in 1995 at the Limerick Unit 1 in Pennsylvania. A manual SCRAM was initiated, during which fluctuating flow and fluctuating current to one of the suction pumps was observed. After the incident

was over, it was observed that a layer of fiber and sludge had formed on the suction strainer causing loss of net positive suction head to the pump that was experiencing fluctuations [1].

After these three events, the US NRC issued a letter, known as Generic Letter 2005-002, to all US operators of Pressurized Water Reactors (PWRs). The letter described the incidents that occurred relating to the clogging of ECCS sump strainers, and it requested that all operators perform an evaluation of the susceptibility of their sump strainers to clogging form LOCA generated debris. Although all prior strainer clogging incidents occurred in BWR's, the NRC questioned the adequacy of the sump strainers in PWRs as they are similar in design and function [1].

The issuance of GL 2004-002 resulted in the NRC opening up generic safety issue 191 (GSI 191). GSI 191 continues to be a challenge for many PWR's that are up for re-licensing from the NRC. The ability to better understand the phenomenology governing debris transport and filtration, and the effects that they have on proper ECCS functionality is the inspiration behind the work presented in this thesis.

In order to better characterize sump strainer and ECCS performance, the stages of a LOCA need to be broken down and better defined. A LOCA, as pertains to GSI 191, can be broken down into 4 main temporal phases: 1) high energy line break (HELB), 2) washdown transport, 3) containment floor debris transport, 4) sump strainer filtration. During the first phase, a coolant carrying pipe fails in some manner characterized as a break. The pipe is carrying high pressure coolant and thus the break is violent and destructive. It is during this phase that the initial LOCA debris is generated in the form of shredded pipe insulation. One of the most common insulation types currently used in PWRs is NUKON fiberglass, and it is this type of insulation that will be used for the experimental studies conducted for this research. The second phase of the LOCA is called the wash down transport phase. During this phase the NUKON fiberglass debris that was dispersed during the pipe break is trapped in the stairwells, walkways, and

gratings found throughout containment. Coolant escaping from the break point cascades onto the trapped insulation, further breaking down the shreds of NUKON, and transporting the now smaller fiber clumps to the floor of containment. The third phase starts at the containment floor level. Once enough coolant has collected along containment floor, the ECCS sump pumps are turned on. Any debris that is entrained within the coolant then starts to transport towards the sump strainers. This is labeled the containment floor debris transport phase. The fourth and final stage of a LOCA occurs at the strainers. The debris that is entrained within the recirculating coolant begins to collect along the sump strainers. Once debris has completely covered the sump strainers, it begins to act as a nonwoven filter. This last phase of the LOCA is known as the sump strainer filtration phase. This sequence is shown notionally in Figure 1 below.
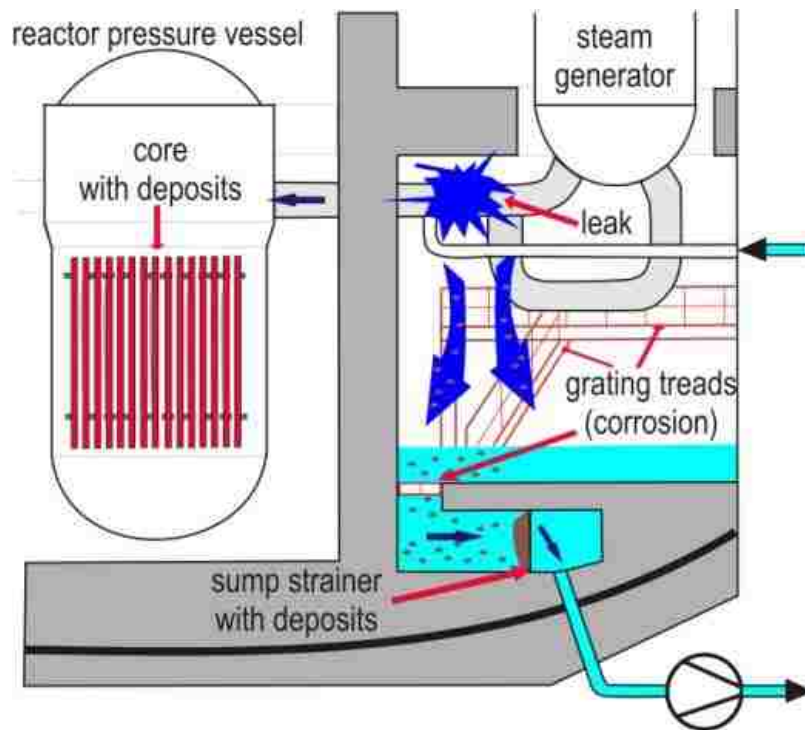

Figure 1: Containment Schematic During LOCA Scenario [2]

Many studies have been done in the past on the fourth stage of a LOCA [2-4]. The effects that corrosion products have on filtration and filtration modeling have been a major topic of study

throughout the history of GSI 191 testing. Tests such as these are labeled chemical effects tests. However, the effects of settling velocity and debris transport that are seen in the third phase of the LOCA are not well understood and there has been no modeling throughout historical tests.

It is this third phase that will be investigated further and is the main focus of this work. The third phase of a LOCA can be further simplified into three separate areas of study: debris settling, suspended debris transport, and tumbling debris transport (transport along the floor). These phenomena are interrelated, and more importantly, all three affect how much debris transports to the sump strainers. It is because of this last part, that further experimentation and model development should be focused on the third phase of the LOCA as this ultimately will help to inform models and tests that are performed studying the fourth LOCA phase.

At this stage it should be noted that there have been tests done in the past on both the settling and the tumbling velocity of fibrous debris (velocity of floor transport) [5,6]. However, all of this testing was done using old fiber preparation techniques.

Various methods have been used throughout the history of GSI 191 testing to mimic the fiber clusters that will arise from a HELB. The first method that was used was called the shredder method, as described in the NRC contractor report 6224 (NUREG/CR-6224) [7]. The shredder method uses an unbaked piece of NUKON fiberglass insulation that is cut into small pieces (3"-6") and then placed into a leaf shredder [7]. The shredder method or some variation of the shredder method was used throughout GSI 191 testing until 2012.

This report also presents a classification scheme to differentiate the sizes of fibrous debris. In the method, fiber clusters are broken down into separate classes based on size. The scale is a visual measuring system and is based on observation and not quantitative measurement. It is still in use today to classify fibrous debris; the different classes are described in Figure 2.
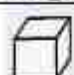
Class		Description
1		Very small pieces of "microscopic" fines which appear to be cylinders
2		Single strand of fiberglass, essentially acts as a suspended strand
3		Multiple attached or interwoven strands that exhibit considerable flexibility
4		Fiber clusters with more rigidity reacting to drag forces more as a semi-rigid body
5		Clumps of fibrous debris which was noted to sink.
6		Larger clumps of fibers. Forms an intermediate between Classes 5 and 7
7		Precut pieces to simulate small debris using manual/mechanical methods

Figure 2: Table Describing Various Classes of Fiber Clusters [5,7]

In 2012 the Nuclear Energy Institute (NEI) published a document titled ZOI (zone of influence) fibrous debris preparation: processing, storage and handling [8]. This document detailed a new method, known colloquially as the "NEI method", of fibrous debris prep which uses a pressure washer in place of a leaf shredder to break down the fiberglass. The procedure starts with baked NUKON sheets, baked NUKON sheets are used to simulate ageing that would happen because the NUKON is in close contact with a hot pipe. The NUKON is weighed to an appropriate batch weight, it is then separated into layers and cut into approximately one inch squares. The fiber is then placed in the bottom of a 5-gallon bucket that has around a half inch of water in the bottom. The fiber is then pulverized with an 1800 psi pressure washer with a 40-degree fan type tip [8]. The tip of the pressure washer is swirled around the bucket to mix the contents while this is being done. The fiber is pulverized for approximately three minutes or until the bucket is close to full. The fiber is then strained and ready to use. The NEI method was used exclusively for GSI 191 testing until late 2014.

It had been noted that the NEI method produced fiber clusters with some sharp corners. This was most likely due to the fiber for the NEI method being cut to one inch squares before being blasted with the pressure washer. Along with sharp edges, some of the clusters in a batch of NEI prepared fiber would be of Classes 4 or 5 (Figure 2). This was considered to be not prototypic of a post LOCA environment and thus an alternate fiber preparation method was needed.

In late 2014 the University of New Mexico (UNM) ran tests on a new fiber preparation technique to be used for GSI 191 testing. This new method is referred to as the "modified NEI method" and differs from the NEI method by how the dry fiber is prepared before pulverization. In the modified NEI method the fiber is kept as one piece and not cut into one inch squares. The fiber is also torn into more layers, eight to twelve for the new method compared to four layers in the NEI method. This new method leads to all of the fiber clusters being Class 1, 2, and 3 with very few, if any Class 4 clusters [3,4].

All of the experiments for this work will be done using the modified NEI method. The results will be compared to some historic data that was collected using older fiber preparation techniques. This data is limited however, because past research focused mostly on the fourth phase of a LOCA, filtration.

This research will focus on the governing phenomena behind fiber transport that occurs during the third phase of a LOCA. The types of debris transport that occur during the third phase of a LOCA are: settling, tumbling, and entrained transport. Each one of these will be explored in more depth using fiber prepared by the modified NEI method. This question is of importance to nuclear reactor safety and the resolution of GSI 191 because the amount and class of fiber that transports to the sump screens can directly affect the filtration phase of the LOCA.

In order to better understand how fibrous debris transports, the governing phenomena need to be broken down into fundamental transport types that can be studied using a series of experiments. The first transport phenomena type is the settling of a single fiber cluster. Settling of individual fiber clusters

can be described by the particle's terminal settling velocity. The terminal settling velocity is dependent on many factors of both the particle and the fluid, and the effects of projected area and thickness on fiber cluster settling velocity will be investigated further.

The second transport phenomenon of interest is that of entrained particle transport. Parameters that affect entrained particle transport are the path to the strainer, the height of the water in the pool, and the critical particle settling velocity. This problem is related to the first because insights gained from experiments answering the first problem can directly be used when calculating critical settling velocity for entrained cluster transport.

The third type of transport phenomenon considered is called tumbling, or sludge transport. This type of transport occurs once fiber has reached the bottom of containment. The fiber clusters that are pushed along the bottom of the floor of containment towards the sump screen are said to be tumbling. It has been shown that a particle's terminal settling velocity is directly correlated to the velocity required to push a particle along the floor of a river bed [9]. This is an interesting connection that could have application towards GSI 191 if it can be proven true for fiber moving along the floor of containment.

In summary it is of interest to the nuclear industry to be able to predict how much fibrous debris is transported to a sump screen during a LOCA. In this chapter, the industry motivation for better understanding these effects was introduced. The Industry methods that have been used to simulate the breakup of fiber have been presented, and one has been chosen as the fiber preparation method for all of the experiments for this research. The types of debris transport have been simplified such that there are three distinct, but related ways that fiber can be transported during the third phase of a LOCA.

Chapter 2 Background Research

There have been many experiments done by universities and industry professionals to assess the debris transport that takes place during a LOCA. Many of the experiments and assessments of debris transport were compiled by the NRC in the form of Nuclear Regulatory Commission Regulation Contractor Reports (NUREG/CR). The most relevant of the NUREGs came out in the mid-1990s where the three that have the most relevant information to the current research are numbered 6224, 6368, and 6772. These three NUREGs build on each other and will be reviewed in order that they were published.

2.1   Summary of NUREG/CR-6224

NUREG/CR-6224 had six total chapters, and the overall reason for the study was to develop a computer code (BLOCKAGE) to estimate head loss for a Mark I containment given a set of initial conditions. The most relevant sections of the 6224 report for this research are the suppression pool transport, and drywell transport sections.

The drywell transport data from 6224 is used to formulate a transport factor, that consists of two terms that are added together. These two terms are the washdown transport factor and the blow down transport factor. Both of these factors are time dependent and vary with break size and break location. These factors were not found experimentally, rather they were estimated using containment drawings, engineering judgment, and data from the Barsebäck I accident [7].

Chapter five of NUREG/CR-6224 is aimed at estimating suppression pool (wet well) transport. The suppression pool transport goes through the same two phases as the drywell transport, blow down and washdown. The suppression pool is connected to the drywell through a number of vents and pipes, and it is from these that debris will be transported. During the blowdown phase the debris is assumed to transport uniformly through the downcomers (partially submerged pipes) [7]. The water in these pipes

will be in the form of steam and will undergo rapid phase change upon contact with the suppression

pool [7]. This phenomenon is called chugging and causes high energy turbulence in the suppression

pool. It is assumed that this turbulence will cause all of the fibrous debris and sludge to be uniformly

suspended inside the wet well.

The washdown transport is assumed to be less uniform and the water is in liquid form during

this phase. No phase change occurs at the exit of the downcomers, and there is far less suppression

pool agitation during the washdown phase. It is assumed that all of the previously suspended debris

starts to gravitationally settle during this phase. The blowdown phase lasts 130 to 150 seconds; the

washdown phase starts after the steam has condensed, and lasts until the startup of the ECCS [7].

The debris transport that takes place during the settling portion of the washdown phase and the

startup of the ECCS is similar to what happens in modern PWR LOCA scenarios. Most current research

uses the experimental techniques from this report as a guide, and the data acquired as a starting

comparison point. One NUREG/CR 6224 experiment in particular is directly comparable to this current

work, the experiment consisted of a mock suppression pool with simulated chugging to suspend fibrous

and particulate debris. After 9.6 minutes the simulated chugging was stopped and the debris was

allowed to gravitationally settle. Water samples drawn from five locations were used to estimate the

settling velocity of the debris via the samples debris concentration [7]. Four tests were conducted, two

using fiber Classes 3 and 4 and two using Classes 5 and 6. The tests using Classes 3 and 4 are the most

applicable to the current work as it is believed that the fiber seen during a LOCA will be of much smaller

size that was originally thought during the testing for NUREG/CR-6224 [3,4].

Settling velocities from the Class 3 and 4 tests range from less than 0.25 mm/s to just under 4.25

mm/s [7]. The values for this test are recorded on a graph with percent of total mass on the y axis and

settling velocity on the x axis (Figure 3). It should be noted that the results from these test are for bulk

settling. This means that fiber clusters that are falling near one another affect each other through

collisions and wake interactions. Also the means by which the settling velocity was recorded varies from

what is normally done in literature [9,10]. Settling velocity of a single particle is measured by timing the

particle falling through a known distance, however this cannot be done for bulk settling. For 6224

testing the settling velocity was the measured by recording the concentration of fiberglass from water

samples taken at staggered heights after a known amount of time had passed.
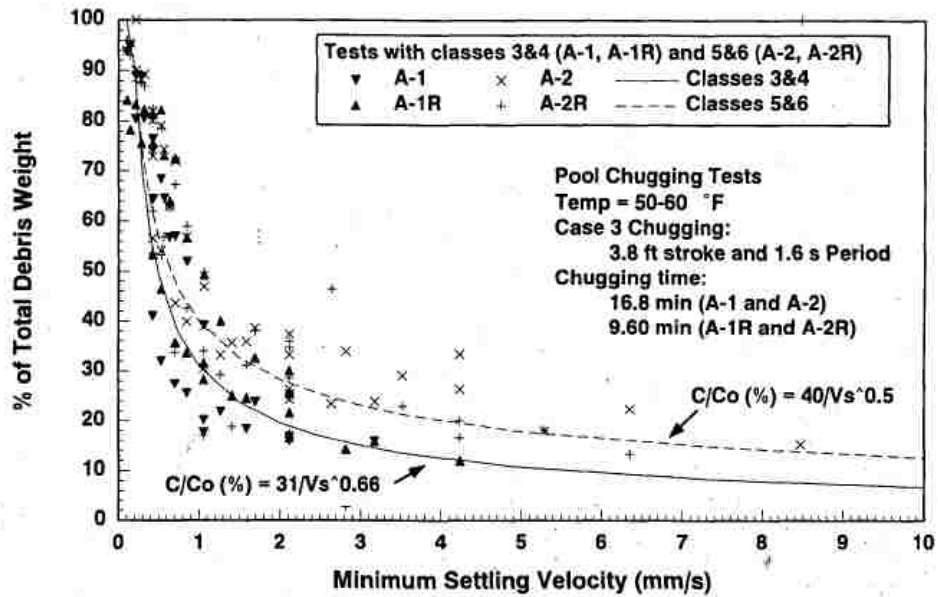
Figure 3: Settling Velocity vs % Total Mass

The conclusion to the debris section of NUREG/CR 6224 was that although the suppression pool

becomes still after the blowdown phase, the pure gravitational settling would be affected by the startup

of the ECCS sump pumps. This led to the conservative assumption that 90% of the fibrous debris

contained within the suppression pool would make it to the sump strainer [7]. No testing was done to

validate the entrained fiber transport fraction in the 6224 report. Investigating the fiber transport

fraction is the overall goal of this current research.

2.2　Summary of NUREG/CR-6368

After the release of NUREG/CR-6224, the NRC designed and performed several more tests to help validate some of the assumptions that were made during the development of the BLOCKAGE computer code. One of these sets of tests that is most interesting to the current research is a set of settling studies performed in a scaled portion of a Mark I containment suppression pool; details of these tests were described in NUREG/CR-6368.

Seven exploratory tests were carried out in order to better inform the test matrix. The final testing matrix consisted of fourteen tests [11]; of those fourteen, three of them are related to this current research. Those are the tests that study the settling of fiber only (no sludge present). Two of the three tests used fiber of Classes 3 and 4, while the last one used fiber of Classes 5 and 6.

The testing procedure for all of the tests was the same. Presoaked fiber was placed in the tank and allowed to let settle. The motor to simulate chugging was then turned on. Chugging occurred for four minutes with water samples being taken every 60 seconds. After four minutes the chugging motor was turned off and samples were taken every two minutes while the fiber was undergoing gravitational settling. The water samples were then used to estimate concentrations of fiber suspended in the liquid [11].

The names of the three tests that are most similar to this research are A-1 R1, A-2 R1, and D-11 R1. A-1 R1 and A-2 R1 have the same chugging period (1.6 s) and mass concentration (0.0032%). The key differences being that A-1 was performed using fibers of Class 3 and 4, while A-2 was performed using Class 5 and 6 [11]. D-11 R1 was performed using fibers of Class 3 and 4, a fiber to water mass concentration of 0.0032%, and a chugging period of 1.9 s [11].

Out of all the data that was recorded for these tests, the most relevant was the settling velocities of the fiber clusters. These tests were performed on bulk batches of fiber as opposed to

individual fiber clusters, for this reason individual settling velocities were not calculated. Instead the

settling velocity versus the percent of total fiber in a test was calculated. The graphs of minimum settling

velocity versus percent of total weight from the four tests are provided in Figures 4 through 6.
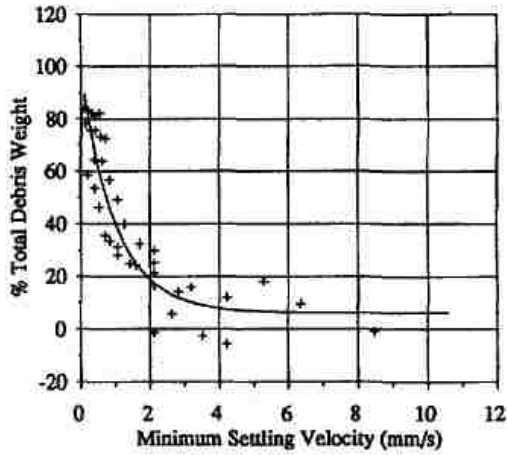
Figure 4: Settling Velocity in A1-R1
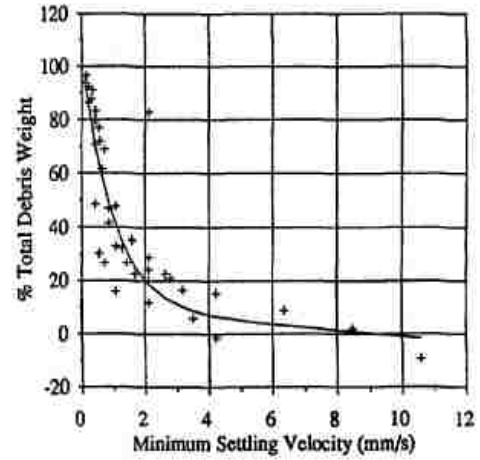
Figure 5: Settling Velocity in A-2 R1
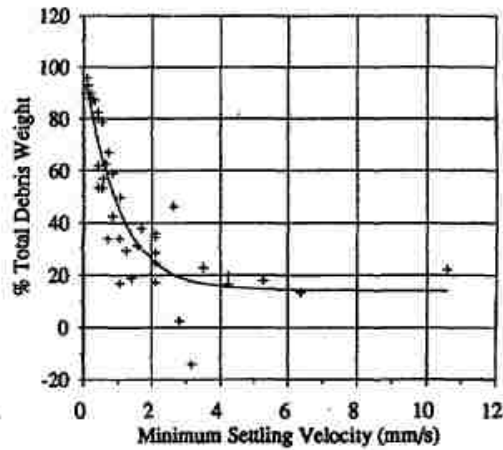
Figure 6: Settling Velocity in D-11 R1

12

Figures 4, 5, and 6 show the percent weight of fiber versus the settling velocity. Each graph has a similar negative exponential trend. More than half of the data points for each experiment lie to the left of the 4 mm/s mark. This gives the first data point with which to compare all future fiber settling tests.

It should be noted that although care was taken to prepare specified fiber Classes for each test, the simulated chugging caused the fiber to break down even further. Investigators noted a considerable amount of single fibers suspended in solution (Class 1 and 2) [11]. This should be taken into account when comparing the results of the current research to the results in tests carried out for NUREG/CR 6368. Although this test is reported to have only Class 3 and 4 fibers, it is possible that the fiber clusters were even smaller.

To this point the NRC had done many experiments but still had a lot of questions left to answer. The big one being how much of this suspended fiber actually transports to the strainer during ECCS start up. The ECCS start up and the chugging phase in the suppression pool overlap. Thus there is a good chance that all of the fiber will be suspended in the pool when the sump pumps are first turned on. The suppression pool transport is also the phase that is most similar to what happens for a loss of coolant accident in a PWR. This makes fibrous debris transport toward the ECCS strainers a key area of interest for both BWR's and PWR's.

2.3   Summary of NUREG/CR 6772

In the coming years, the NRC put out many more NUREG's that studied various aspects of GSI 191. NUREG/CR 6772 summarized separate effects transport tests that were performed on various forms of containment insulation [12]. Separate effects tests are any form of testing in which only one aspect of the accident scenario is studied. In this case, the individual transport characteristics of various types of debris were tested. Tests that study more than one aspect of the problem, such as transport and filtration, are labeled integral effects tests.

NUREG/CR-6772 detailed experiments that were performed to gain better understanding of the transport characteristics of several common types of LOCA generated debris. The tests that were performed on NUKON fiber glass are the only ones of relevance for this current research. The relevant characteristics that were tested for NUKON are: terminal settling velocity in still water, terminal settling velocity in flowing water, incipient tumbling velocity, bulk tumbling velocity, open channel transport distance, and screen retention velocity. All of the tests were performed in the separate effects large and small flumes at the University of New Mexico [12].

Before the official tests were conducted, some exploratory tests were performed. Of these tests, three are relevant to this research. They are: the water temperature effects on NUKON, effect of flume water height on debris transport, and effect of surface roughness on fiber transport.

The tests for temperature effects on NUKON determined that soaking the shredded fiber in an 80° C water bath for 10 minutes treated the fiber in a way which would cause it to readily sink in still pools. Fiber that was not soaked in the bath would readily float on top of the water even when forcibly submerged. Thus all subsequent fiber used for testing was presoaked in water before being used in a test. It was also determined that the water temperature used for settling velocity tests had no effects on the fiber so long as it was presoaked in hot water before the test [12].

The effect of flume water height was tested by repeating transport experiments at three different water depth ranges: 3 inches, 8-12 inches, and 24 inches. No sufficient variation was observed in the tests performed at the three depths, therefore it was concluded that all subsequent tests performed in the large flume used a water depth of 18 inches [12].

The effect of the flume surface roughness on fiber glass transport was tested by performing a series of experiments with two different false bottoms in place in the flume. The smoother of the two bottoms was acrylic, with smoothness similar to painted concrete (often found in containment). The

rougher of the two bottoms was constructed of plywood. The incipient and bulk tumbling velocities of

NUKON fiber glass were tested using both surfaces. The results showed that there was no statistically

significant difference between the two surfaces [12].

The NUKON fiberglass that was used for flume and settling tests was prepared using an air jet.

This method is different than what was done in the past (shredded), and resulted in fibers of mostly

Classes 3 and 4. As was mentioned earlier, all of the fiber that was used in flume and settling tests was

presoaked in 80° C water for at least 10 minutes. The results from both the flume tests and the settling

tests can be seen in Figure 4.

Table 3.1 Summary of Measured Nukon Transport Properties			
Fragment Size:	6-in.	4-in.	1-in.
Settling Velocity (ft/s)	0.41	0.40	0.15
Inlet Flow Conditioning:	Configuration A	Configuration B	Configuration C
Incipient Tumbling Velocity (ft/s)	0.12	0.07	0.06
Bulk Tumbling Velocity (ft/s)	0.16	0.09	0.10
Lift-at-the-Curb Velocity (ft/s)			
2-in. curb	0.25	0.25	0.22
6-in. curb	0.34	0.25	0.28

Figure 7: Results from NUREG/CR-6772 [12]

The three inlet flow configurations that are cited in Figure 7 were used to represent different

possible conditions found inside containment in a post-LOCA scenario. Configuration A was labeled

diffused flow entry, which represents calm pool conditions that can be found in containment far from

falling break flows. It used a flow conditioning section which consisted of damping pads and a flow

straightener to create uniform flow inside the flume. Configuration B was labeled free-fall flow entry,

which incorporated the same configuration as was used in configuration A, but with the damping pads

removed. Flow still passes through a straightener, but the eddies and turbulence caused by the return

water striking the flume surface made for rough test conditions. This configuration better represents areas of containment near the break flow. Configuration C was labeled immersed pipe flow entry. This configuration was the same as configuration B except now the pipe was immersed under the surface of the water in the flume [12]; the pipe diameter was also decreased from 10-inch nominal to 6-inch nominal. This configuration led to similar flow pattern as in configuration B, but with slightly less turbulence from the lack of surface interaction effects.

In order to compare the data from NUREG/CR-6772 with that of the other NUREG's and settling tests, the data in Figure 7 was converted to metric and can be seen in Figure 8.

Summary of measured NUKON Transport Properties (metric)			
Fragment size (mm)/(Class)	152.4/>7	101.6/>7	25.4/3&4
Settling Velocity (mm/s)	124.97	121.92	30.48
Inlet Flow Condition	Diffuse (A)	Free Fall (B)	Immersed (C)
Incipient Tumbling Velocity (mm/s)	36.58	21.34	18.29
Bulk Tumbling Velocity (mm/s)	48.77	27.43	30.48

Figure 8: Results from NUREG/CR-6772 Metric [12]

From Figure 8 it can be seen that the settling velocity data from the separate effects small flume is larger than that found in the chugging tests from NUREG/CR-6368. The reasons behind this are not known, but it should be noted that the preparation procedure and methods of measuring used in both tests were different. Also the tumbling velocity for both bulk and incipient tests follows a similar trend, in which the average tumbling velocity being impacted by the inlet flow condition. The average velocities needed to initiate tumbling are higher for the diffuse inlet condition when compared to free falling and immersed inlet conditions. This is to be expected as the added turbulence from the latter two inlet conditions helps lift the fiber off of the floor of the flume and aids in tumbling transport.

2.4   Summary of Texas A&M Settling Research

Researchers in the Nuclear Engineering department at Texas A&M University (TAMU) were the next to run experiments regarding the transport characteristics of NUKON fiberglass [5]. The objective of the tests they performed was to explore the effects of temperature on the free settling rates of individual NUKON fiber clusters. The results from the settling tests that were performed at room temperature can be used for comparison to the current research.

Shredded NUKON was used in the tests done at TAMU. They performed separate tests on both Class 4 and Class 5 fragments of NUKON. The results from the Class 4 and 5 tests can be seen in Figures 9 and 10 respectively. These tests were carried out in a 40.64 cm diameter water column with a length height of 243.84 cm [5]. The water temperature for the room temperature runs was between 24° and 26° C [5].
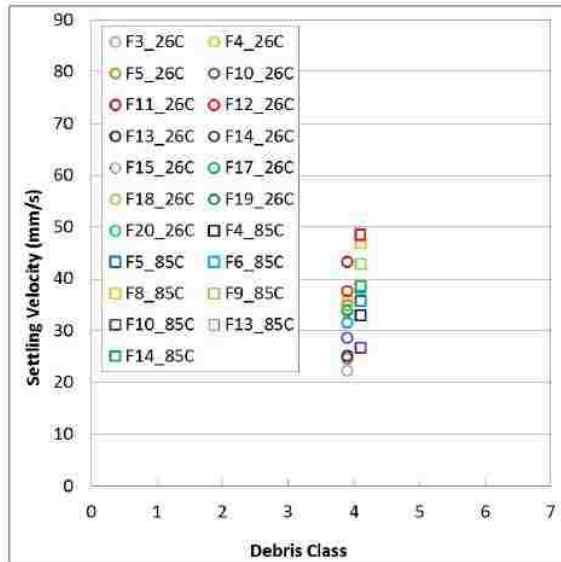
Figure 10: Settling Velocity of Class 4 Fragments [5]
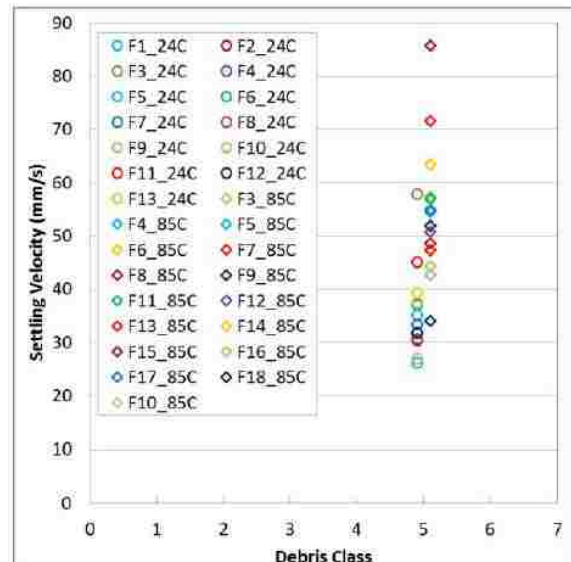
Figure 9: Settling Velocity of Class 5 Fragments [5]

Lee et al. made the distinction that NUKON fragments behave similar to falling disks [5]. Disk like behavior was observed during the elevated temperature settling tests of Class 5 fragments. The lower

viscosity of the water affected the Class 5 fragments more than the Class 4 fragments. This trend is also

seen when studying disks of increasing diameter, therefore the conclusion can be made that fiber

fragments act like irregular disks when free settling (see Figure 9 and 10). The Class 5 fragments were

noticed to have a smaller ratio between their largest cross sectional diagonal length and their thickness.

This leads the Class 5 fragments to behave more like falling disks, while Class 4 fragments behave more

like falling spheres. They concluded that temperature of the water does affect the fall velocity of fiber

fragments (Figure 9), and that different drag coefficients are needed based on what Class of fiber is

being studied [5].

Lee et al.'s work is significant because it is the first time that researchers have attempted to

compare the settling velocity of fiber fragments with that of similar objects. This marks the first time

where predictive capabilities are attempting to be introduced into the problem of LOCA generated

debris transport. That is, correlating a Class of fiber to a possible Reynolds number or particle settling

velocity.

2.5   Background Summary

All settling velocity data has now been presented for NUKON fiberglass. For comparison, all the data has been compiled in one chart and can be seen in Figure 11.

Summary of Settling Velocity Data			
reference	fiber Class	preparation	average settling velocity (mm/s)
Lee et al.	4	shredded	32.2
Lee et al.	5	shredded	35.6
6224	3 to 6	shredded	< 4
6368	3 & 4	shredded	~ 2
6368	5 & 6	shredded	~ 2
6772	3 & 4	air jet	30.48

Figure 11: Summary of Settling Velocity Data from 6224, 6772, and Lee et al. [5,7,12]

From Figure 11 it can be seen that the settling velocity data for NUKON that was collected using calm pools is slightly above 30 mm/s, while the settling velocity for fiberglass in agitated pools was less than 4 mm/s. This is most likely due to the fact that significant breakdown the fiber was noted during the agitated pool tests. The breakdown of the fiber clusters leads to significantly lower settling velocities because less massive particles tend to fall slower than more massive particles.

What is not included in Figure 11 is the data for clusters much larger than Class 7. The tests performed for NUREG/CR-6772 used a batch of fibers with diameters around 4 inches and another batch of fiber with diameters around 6 inches. These tests were omitted in the figure because it is believed that fibers that large are not prototypic to a LOCA scenario.

Based on the information presented from previous research, two needs are obvious: past fiber cluster measurement techniques are inadequate in capturing information useful to settling velocity predictions, and no equation or correlation exists that can predict the settling velocity of a fiber cluster.

Chapter 3 Theory

3.1   Introduction

The determination of the settling velocity of particles based on particle (or cluster) size and shape has many scientific and engineering applications. The settling velocity for spheres based on their diameter and density was first correlated by Stokes, and is now well-documented as a valid solution to the free settling of a sphere at low Reynolds numbers. It is commonly referred to as Stokes law. Since then, many researchers have been interested in similar solutions for particles that are non-spherical. Through the research presented in this thesis, a correlation was developed for the drag coefficient of clusters of NUKON fiber using only the dimensions and physical properties of the cluster.

3.2   Hydrodynamic Principles

The drag correlation that is developed in this thesis, and the correlations that are referenced in literature are based on fundamental fluid dynamic principles. In order to better understand the principles that are present in this problem, a free body diagram of a fiber cluster at terminal velocity is presented in Figure 12.
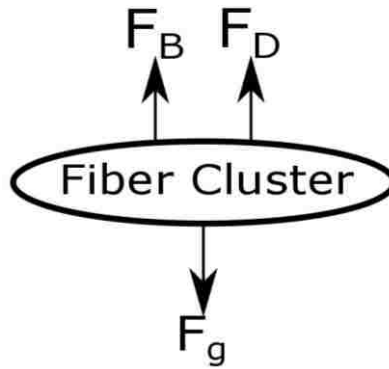
Figure 12: free body diagram of fiber cluster at terminal settling velocity

Performing a force balance on the particle (assuming up is positive) leads to the following equation.

$$\sum F = 0 \quad \Rightarrow \quad F_D + F_B - F_g = 0 \qquad (1)$$

From analysis of the free body diagram and the force balance it is clear that there are three forces of interest acting on the particle once it reaches terminal velocity: drag, buoyancy, and gravity.

The first term of equation 1 is the drag force, which is the force that opposes the relative motion of an object in a fluid. As it concerns terminal settling velocity, it can be broken down into two types: form drag, and skin friction. The drag coefficient is the dimensionless proportionality constant that arises in the drag equation, which relates the drag force exerted onto an object to the relative velocity, fluid density, and projected area of the object (equation 2). The type of drag that most effects a body is dependent on the shape of that body. Slender bodies such as airfoils, rods, and wings develop drag mostly from skin friction. Blunt bodies such as spheres, disks, and cubes develop drag mostly from stagnating fluid on the face of the body. Either type of drag is taken into account through use of a drag coefficient, however the fiber clusters that are the focus of this research resemble disks when settling [5]. It is thus noted that the drag developed by these particles is mostly of the form drag type. The drag equation is defined as follows:

$$F_D = \frac{1}{2}\rho u^2 C_D A \tag{2}$$

where F_D is the drag force, u is the relative velocity of the particle, A is the projected area of the particle, and ρ is the fluid mass density. The drag coefficient (C_D) can be solved for by rearranging equation 2 as follows:

$$C_D = \frac{2F_D}{\rho u^2 A} \tag{3}$$

The second term of Equation 1 is the buoyant force which arises when an object is submerged in a fluid, from the difference in hydrostatic pressure acting on the top and bottom of the object. Using Archimedes principle, the buoyant force is equal to the weight of the fluid that is displaced by the object. This can be written as follows:

$$F_B = \rho g V \tag{4}$$

where F_B is the buoyant force, g is the acceleration due to gravity and V is the volume of the particle.

The last term in equation 1 is the force due to gravity, which is well known to be the mass of the object multiplied by the acceleration due to gravity. If the particles of NUKON fiberglass are assumed to have uniform density, then we can replace the mass term with the density of the particle multiplied by the volume of the particle. This leads to the following equation for the gravitational force acting on the particle.

$$F_g = \rho_p g V \tag{5}$$

where F_g is the force due to gravity, and ρ_p is the density of the particle.

The clusters of NUKON fiberglass that are the focus of this thesis approach terminal settling velocity within the first few seconds of settling. Under this assumption, the relative velocity term in equation 3 can be replaced by the terminal settling velocity for the cluster. At terminal settling velocity

the force term in equation 3 can also be replaced by the force due to gravity minus the buoyant force acting on the particle.

Calculating the volume of a non-isometric particle can prove difficult, and for this research the volume of the particle is calculated by multiplying the projected area of the particle by the average height of the particle. Both of these measurements are taken visually through the use of a camera and grid squares. Making the substitution for volume in equation 4 and 5 leads to the equations for buoyancy and gravity in terms of parameters that can be measured during experiments. The substitutions can be seen in equations 6 and 7 respectively.

$$F_B = \rho g A h \tag{6}$$

$$F_g = \rho_p g A h \tag{7}$$

Equations 6 and 7 now have very similar forms, the only difference being that the gravity term uses the particles density while the buoyancy term uses the fluids density.

Substituting equations 6 and 7 into equation 1, solving for F_D, and factoring out like terms leads to an equation for the drag force that is only in terms of experimentally measured parameters.

$$F_D = g A h (\rho_p - \rho) \tag{8}$$

Substitution into the equation for drag coefficient leads to the equation that will be used to measure the experimental value for drag coefficient of tested fiber clusters. Note that equation 3 has a projected area term in the denominator that will cancel with the projected area term stemming from the volume calculation.

$$C_D = \frac{2gh(\rho_p - \rho)}{\rho u^2} \tag{9}$$

23

Equation 9 will be used to calculate the actual drag coefficient for comparisons with the predicted drag

coefficient, and to solve for the settling velocity from predicted drag coefficient values once the

correlation has been calibrated.

The Reynolds number is another dimensionless number that is used throughout literature as a

way to characterize the flow regime of a particle. It is defined as the ratio of velocity multiplied by length

to viscosity. It is also used as an input for the correlation developed in this thesis as well as in other

correlations throughout literature. It is defined in the following equation.

$$Re = \frac{\rho u L}{\mu} = \frac{u L}{\nu} \tag{10}$$

where μ and ν are the dynamic and kinematic viscosities, respectively, and L is the characteristic length

of the particle. In previous studies, fiber clusters have been shown to be largely amorphous in shape

[5,7], so determining proper dimensions (such as characteristic length) is difficult. The following

equation was used to calculate the characteristic length of fiber clusters for two reasons: it uses particle

projected area and perimeter which are easy to measure for fiber clusters, and when used on well-

known shapes the equation reduces to the standard parameter (IE the diameter for spherical or disk

shaped particles).

$$L = 4\frac{A}{P} \tag{11}$$

where A is the particle projected area and P is the particle projected perimeter. Using equation 5, the

characteristic length of a sphere or disk is the diameter, and for cube or thin square it is the side length.

3.3   Non-Isometric Settling Background

Non-spherical particles can be categorized as either isometric or non-isometric. Isometric

particles have equal dimensions about at least one given axis; examples include cones, cubes, rods, and

pyramids. Non-isometric particles are asymmetric and tend to have a random shape, making them more

difficult to characterize. Some examples of particles that exhibit non-isometry are rocks, sand, and sedimentation flocs. The correlation presented in this thesis is rooted in work presented in non-isometric literature, based on the amorphous nature of the fiber clusters in this study.

One of the first researchers to perform settling velocity work with non-isometric particles was Arthur T. Corey [9], whose work studied how particle shape affected the falling velocity of sand grains. Two aspects of Corey's research are relevant to this work: particles tend to fall so that the resistance against its face is a maximum [9] (which provides some insight of the flow regime), and the velocity required to move particles along the bed of a river is directly related to the settling velocity of the particles [9]. These principles, while originally applied to sediment transport within river beds, can also be applied to the transportation of clusters of NUKON fiber along the containment floor.

Corey listed five variables that were of importance for the development of his correlation: net gravitational force, fluid viscosity, particle terminal velocity, particle projected dimensionality, and particle surface curvature. The main problems that irregular shaped particles, such as sand grains and fiber clusters, pose is that shape and curvature dimensions are difficult to determine. Corey developed a shape factor that is easier to measure for sand grains, and can be used in place of more complete measurements. Surface area and volume are the ideal particle characteristics, but can be tedious if not impossible to measure for non-isometric particles.

The Corey shape factor (CSF) is based on the three mutually perpendicular axes of the particle: major (a), intermediate (b), and minor (c). Corey proposed that the most important shape factor that can be made from these three measures is the flatness, which is expressed as:

$$CSF = {}^{c}\!/_{\sqrt{ab}} \qquad\qquad (12)$$

He also noted that the use of flatness as a shape factor is not as complete or descriptive as using volume

ratios or surface area ratios, but is much easier to measure for particles that are rough and irregular [9].
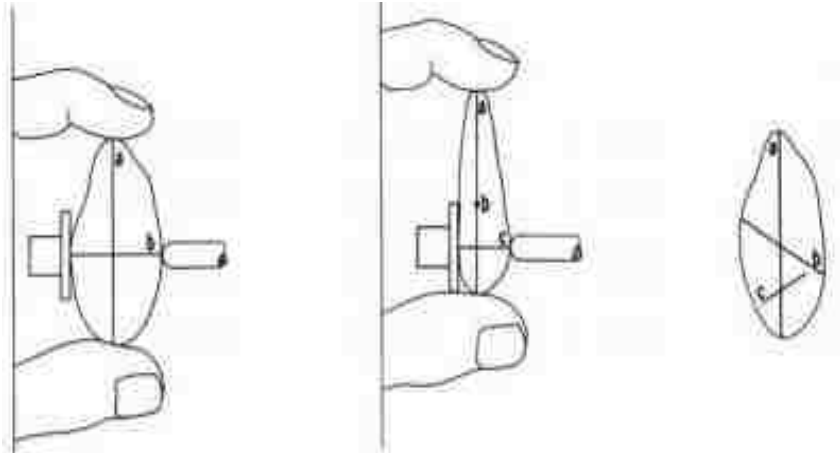
Figure 13: Corey Shape Factor Measurements

Using a low speed camera and a strobe light, Corey collected settling data for particles with CSF

values ranging from 0.21 to 0.95. These points were plotted on graphs with drag coefficient along the

vertical axis and Reynolds number along the horizontal axis (Figure 14). Two reference lines were also

plotted, one for spheres and one for thin discs. When the irregular particle settling data was overlaid

onto the reference lines, it was shown that as the CSF approaches 1.00, the particle behaves like a

sphere and its settling velocity approaches that of a settling sphere. The data was also plotted with drag

coefficient along the vertical axis and CSF along the horizontal axis for particles in different Reynolds

ranges. These plots exhibited a negative exponential behavior that differed slightly between Reynolds

ranges (Figure 15).
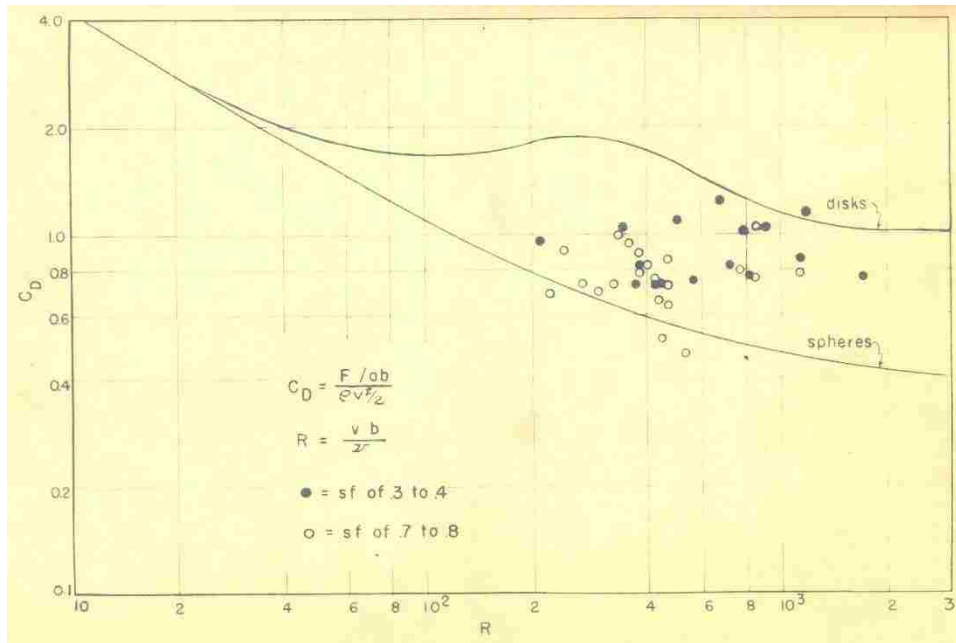
Figure 14: Reynolds vs. Drag for Corey's Thesis [9]
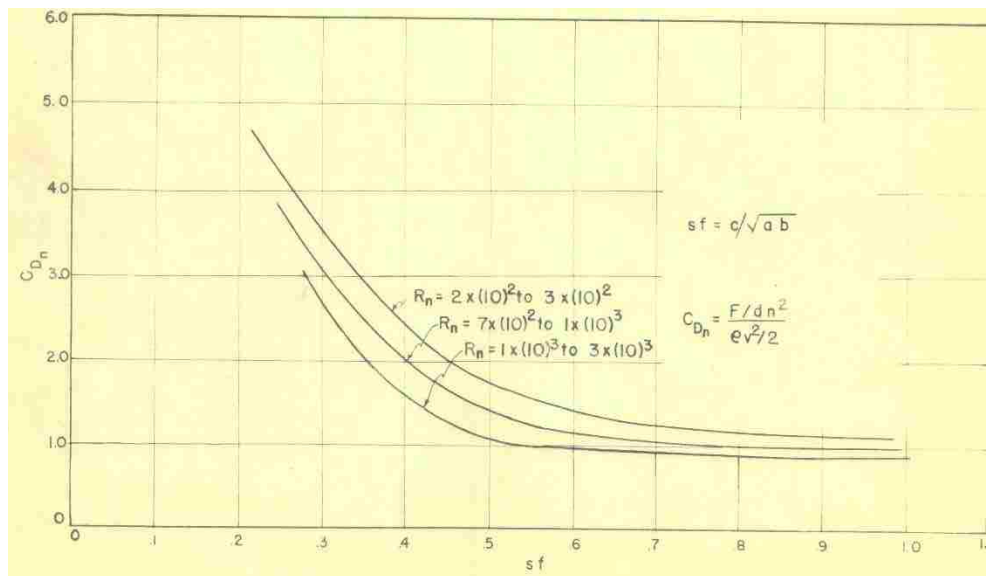
Figure 15: CSF vs. Drag for Corey's Thesis [9]

Corey never proposed a numerical correlation, but his work on particle measurement and relating shape factor to drag coefficient were important contributions to the understanding of non-isometric particle settling.

27

The developed correlations of Cheng [13] and Camenen [14] took a similar approach to determining settling velocity. They studied particles of sand, and used the same base equation with which to base their correlations on. This form was derived from the two boundary conditions at either extreme of the Reynolds scale. For low Reynolds numbers, settling takes the form of the Stokes equation, and the drag coefficient is inversely proportional to the Reynolds number. At high Reynolds numbers, the drag coefficient tends toward a constant. By combining these two patterns, a base equation relating drag coefficient to Reynolds number can be formulated and was used by Cheng and Camenen as a starting to point for their proposed correlations. The equation takes the form:

$$C_D = [\left(\frac{A_*}{Re}\right)^{1/n} + B^{1/n}]^n \qquad (13)$$

In equation 7, A and B are constants; A is dependent on the shape of the particles that are being studied, and B is the lowest limit of the drag coefficient for the particles being studied. The exponent n is an empirical constant that was determined through linear regression performed on historical data for the falling velocity of sand grains [13,14].

The correlations of Cheng [13] and Camenen [14] both start with the same form of the Reynolds-to-drag correlation, but differ in the methods used to determine the constants A, B, and n. Cheng uses historical data for both A and B. In literature, A=32 appears in almost all papers dealing with low Reynolds settling, and the value for B was set by the lowest drag value found in literature, B=1 [13]. The value for n was found by averaging values that were used by previous researchers for sand particles; Cheng used a value of n=1.5. Substituting these values into equation 4, Cheng's correlation can be written as:

$$C_D = [\left(\frac{32}{Re}\right)^{1/1.5} + 1]^{1.5} \qquad (14)$$

Camenen used calibration equations based on the CSF and a roundness factor represented by the variable P to determine the constants A, B, and n. The roundness is a shape factor used to measure sand that varies from 0 (for perfectly angular particles) to 6 (for perfectly round particles). The use of calibration equations can lead to better results than use of historical data because the constants are based on measurements from the particles that are being studied. It can also be more tedious because the constants in the equation vary based on the values for roundness and CSF. Camenen provided values for common types of particles [14], however, care will need to be taken when using the calibration equations on NUKON fiber clusters. The calibration equations for A, B, and n are listed below.

$$A = a_1 + a_2[1 - \sin(\frac{\pi}{2}CSF)]^{a_3} \tag{15}$$

$$B = b_1 + b_2[1 - \sin(\frac{\pi}{2}CSF)]^{b_3} \tag{16}$$

$$n = n_1 \sin^{n_2}(\frac{\pi}{2}CSF) \tag{17}$$

where

$$a_1 = 24, \quad a_2 = 100, \quad a_3 = 2.1 + 0.06P$$

$$b_1 = 0.39 + 0.22(6 - P), \quad b_2 = 20, \quad b_3 = 1.75 + 0.35P$$

$$n_1 = 1.2 + 012P, \quad n_2 = 0.47$$

Based on the work that Cheng and Camenen performed regarding the settling rates of non-isometric particles, the formula for drag coefficient (equation 14) was modified to match settling data for fiber clusters. Cheng and Camenen worked mostly with natural particles of sand and sediment which are denser and have higher sphericities than the clusters of NUKON fiberglass that were tested in this work.

The non-isometric settling was used as a basis for the development of a predicative correlation. The work of Willmarth et. al [15] on the settling of disks is used to compare the wake behavior of the fiber clusters to that of disks. When measured, fiber clusters resemble amorphous disks [5], thus it is hypothesized that the wake behavior will be similar.

There were three characteristics of the disks that were observed by Willmarth that will be used in the comparison study with fiber clusters. The first characteristic was that disks above Reynolds numbers of around 50, oscillated [15]. These oscillations were one of three types: damped, undamped, or boundary. The amplitude of the oscillations of the damped samples were reduced during the time they were falling. The amplitude of the oscillations of the undamped samples increased during their fall, and the amplitude of the boundary disks neither increased or decreased.

Willmarth noted that whenever the disks would oscillate, they would translate through the water in the opposite direction of the oscillation [15]. This oscillation followed by translation makes the disks fall in a zig-zag pattern. This fall pattern will be compared to the fall pattern of fiber clusters.

The final observation, made by Willmarth was the shape and characteristics of the wake vortices formed behind the disks. The vortices that were formed behind the disks ranged in shape from horseshoe to circular. The vortices were formed every time that the disk translated after an oscillation [15]. The formation of these vortices differs in the formation of a Karman vortex street. The oscillations behind the disks are caused by the oscillation and translation, where a Karman vortex street is caused by wake instabilities behind the object. Thus the vortices behind the disks start to form and oscillate at lower Reynolds numbers than are seen in a Karman vortex street.

3.4   Correlation Development

The hydrodynamic behavior that makes equation 13 applicable to sand and sediment particles is still valid for the fiber clusters in this study, though the coefficients A, B, and n must be determined

using data for the settling of fiber clusters. The length term used for the Reynolds number was adjusted

due to the measuring difficulties that are imposed by the fiberglass. For hard particles, like sand, the

diameter is typically chosen by using the CSF or the sieve diameter. This is not possible for fiber clusters

due to their highly flexible and porous nature.

Several assumptions must be stated and validated in tandem with the adjustments to the

constants in order to use equation 13 to predict the drag coefficient of fiber clusters. The main

difference between fiber clusters and other types of sediment is the relative porosity of the particles.

Fiberglass insulation has high porosity values by design, which leads to difficulties when trying to

calculate the density of the particles, and the stagnation pressure on the particles' leading face. The drag

coefficient cannot be accurately calculated without considering the possible flow through the porous

particle. Based on the differences between porous particles and sand, the underlying equations for drag

coefficient and Reynolds number were derived, and a new correlation based on equation 13 is

presented.

The density of a porous particle that is settling can be difficult to calculate, as the density of the

solid fibers and the porosity of the particle must be accounted for. After preliminary testing and data

analysis, the particle density term was chosen to be equal to the product of the solid fraction of the

particle and the density of the individual fibers plus the porosity of the cluster times the density of the

fluid. The solid fraction was calculated by subtracting the porosity from unity. Practically speaking, this

means that the particles are approximated as solid masses with a density that is a combination of the

density of the glass fibers and the density of water. The equation used for the particle density is:

$$\rho_p = \phi\rho + (1 - \phi)\rho_f \tag{18}$$

where ϕ is the particle porosity, and ρ_f is the density of the individual glass fibers. In this instance, it is

assumed that the porosity of a fiber cluster is the same as the fabricated porosity of bulk fiberglass. This

assumption is reasonable based on the preparation method of the fiber. The pressure washer breaks

large sheets of NUKON down into smaller clusters, but individual clusters are still held together in a state

that is similar to when the fiberglass was initially manufactured.

In order to implement equation 3 for the drag coefficient of a particle, it must be assumed that

the fluid in question is not flowing through the particle, because the projected area of the falling particle

plays an important role in the determination of the drag coefficient. For solid particles, the flow

stagnates on the leading face and then is forced around the particle; for particles that are porous, there

is a possibility that the pressure difference between the leading and trailing faces of the particle will

induce flow. If the particle in question has flow passing through it, then the area where the fluid is

stagnating is not equal to the measured projected area.

Flow through a porous medium has long been a topic of study for geologists and environmental

engineers. Darcy's law can be used to calculate the flow of fluid through a porous medium. It is a

function of the permeability of the medium, the pressure difference between the two sides of the

medium, the length over which that pressure drop takes place, and the viscosity of the fluid flowing

through the medium. The velocity form of Darcy's law can be seen below.

$$u_t = \frac{\kappa}{\mu} \frac{\Delta P}{h}$$
(19)

where κ is the permeability of the fiber cluster, u_t is the velocity of the fluid through the particle, and ΔP

is the pressure difference between the leading and trailing faces of the particle. The Darcy equation

presents two new unknown terms that must be solved for, the pressure difference and the permeability

of the particle. The pressure difference can be solved by utilizing the dynamic pressure term in

Bernoulli's equation, while determining the permeability is more complicated. Permeability is typically

used to measure the flow through packed beds of rock or sand for filtration purposes. The units of

permeability are m^2 (also known as a darcy). Permeability arises as a proportionality constant in the Darcy equation, similar to the drag coefficient in equation 2.

Solving for the permeability of a cluster is not something that is often done. Kim and Stolzenbach [16] ran into a similar problem while studying the permeability of synthetic fractal aggregates. They review many different analytical permeability functions that can be used to solve for the permeability of a substance when the void fraction and particle radius is known. Most of these permeability functions are based on experiments that utilized spherical or near spherical particles. However, two of the correlations used cylinders instead of spheres as a medium for their experiments. One was based on a woven pattern of cylinders, while the other was based on a random orientation of cylinders. The fiberglass that is used for these tests has randomly laid cylindrical fibers, and thus the second of the correlations for cylinders is chosen for the calculation of permeability.

$$\kappa = \frac{r^2}{16\phi_*^{1.5}(1+56\phi_*^3)} \tag{20}$$

where r is the radius of the fiberglass cylinders and ϕ_* is the solid fraction of the particle.

Now that an expression is known for finding the permeability of the fiber clusters, the pressure differential must be found for use in Darcy's law. The most straightforward way to do this is by using the equation for dynamic pressure stemming from Bernoulli's equation, which can be expressed as:

$$\Delta P = {^1\!/_2}\,\rho u^2 \tag{21}$$

Using equations 19, 20, and 21, the velocity of the water flowing through the settling fiber cluster can be calculated. The physical characteristics for NUKON fiberglass are presented in Figure 16. Using this data, the velocity of the water flowing through the fiber cluster was calculated for each sample with a maximum value of 0.1327 mm/s, and a maximum flow ratio of 0.6749%. With a maximum flow ratio of

less than one percent, the flow through the particles can be neglected and the no-flow assumption

holds true.

Properties of NUKON Fiberglass	
Fiber Density (g/cm^3)	2.55
As Fabricated Porosity	0.99
Fiber Diameter (µm)	7.00

Figure 16: Properties of NUKON Fiberglass [5]

The fiber cluster is now treated as a solid amorphous particle with flat faces. Under this

assumption, equation 13 is adapted to fit the data for the settling of fiber clusters. The constants

coefficients A, B, and n were determined through experimentation performed using a settling column,

and are presented in a subsequent chapter.

Once the coefficients for equation 13 are determined, the equation can be used in an iterative

manner to solve for the settling velocity of a particle when the dimensions of the particle are measured

(projected area, projected perimeter, and average height). Some substitutions to both equation 3 and

equation 21 are made such that the iterative process is simpler.

First, substitution of equation 11 into equation 10, and the subsequent substitution into

equation 13 gives an expression for the drag coefficient in terms of measureable parameters and the

particle velocity.

$$C_D = \left[\left(A_* \frac{vP}{4uA} \right)^{1/n} + B^{1/n} \right]^n \tag{22}$$

Substituting equation 18 into equation 9 yields a solution for the drag coefficient in terms of

measureable parameters and the particle velocity, noting that the solid fraction is equal to one minus

the porosity.

$$C_D = \frac{2gh(1-\phi)(\rho_f - \rho)}{\rho u^2} \qquad (23)$$

Using equations 22 and 23, the settling velocity for the fiber clusters can be estimated, based on the projected area and average height (both measureable quantities) of the clusters. Once the area and height are measured, they are substituted into equation 22, along with an estimated settling velocity. Substituting the drag coefficient from equation 22 into equation 23, a new settling velocity is found. This new velocity is then used to recalculate the drag coefficient, and this process is repeated until the value for settling velocity converges.

Using these two equations iteratively for many particles can prove to be time consuming and tedious. Instead of having to measure the area, perimeter, and height for all particles of interest, it is easier to classify a particular preparation method statistically. This can be done through dimensional analysis of a statistically significant sample of fiber clusters from a specific preparation technique. Once a distribution of fiber sizes has been determined, equations 22 and 23 are used to transform the size distribution into a settling velocity distribution.

Chapter 4 Experimental Procedure and Apparatus

4.1   Methodology

Tests were performed in order to calibrate and validate the correlation developed in chapter 3. The testing was performed in a column of still water at room temperature. The time it takes a cluster to fall a pre-determined distance was recorded and used to calculate the terminal settling velocity of the cluster.

The data that was collected from settling tests was used to calibrate the constants for the drag correlation described in Chapter 3. Each fiber cluster was measured using 1 mm grid sheets that were placed onto a measuring station. Images of the fiber cluster were taken from the top, right, and front

positions of the measuring station. These images were used to calculate the projected area, projected perimeter, and average height of each fiber cluster.

Once the drag correlation was calibrated it was used to estimate the settling velocity of individual fiber clusters, or the settling velocity range for a batch of fiber, if the size range is known. The drag correlation was calibrated using linear regression with the data from experiments. The lowest accepted experimental value for the drag coefficient of a cluster was used as the value for the drag limit.

Dye tests were run to better understand the wake formation behind a falling fiber cluster. Still images from dye tests were used to compare the wake developed behind a fiber cluster to that developed behind a disk.

4.2   Apparatus

There were three main apparatuses used for the settling tests performed for this research. The first was a fiber preparation apparatus, the second was a fiber measuring station, and the third was the settling column. Fiber was prepared in bulk first, then individual fibers were measured using the metric station, and finally they were used in settling velocity tests performed in the column.

The fiber preparation apparatus consisted of a 5-gallon bucket, an 1800 psi pressure washer, and a 40 μm mesh sieve (Figure 17). Post processing was performed using a stir plate, stir bar, stir rod, and 2-liter glass beaker. The fiber preparation was completed near a floor drain and hose such that the water used can be drained easily, and so that it was readily available for the pressure washer. The post processing was done in a chemistry lab with access to a stir plate and appropriate equipment.

The cluster measuring station was constructed of 3 2-inch by 2-inch polycarbonate squares that were glued tougher to form the corner of a cube (Figure 18). One mm square grid stickers were placed on each surface as a means to measure the size of the fiber clusters. Fiber clusters were placed in the

center of the bottom square and photos were taken of the top, right, and front sides of the fiber

clusters. The projected area, projected perimeter, and average height of the fiber cluster were

estimated from the photos using the grid squares.

Figure 17: Fiber Preparation Apparatus

A still water column was used to test the terminal velocity of the clusters. The column was made

out of a piece of transparent acrylic tube fastened to a pipe flange and was sealed using O-rings. The

column was 15.24 cm in diameter and 152.4 cm in length with the fiber clusters falling for 30 cm before

the timing begins to ensure that they are at terminal velocity. After 30 cm there is a ring of masking tape

to mark when timing begins, and 100 cm below that ring there was another ring of masking tape to

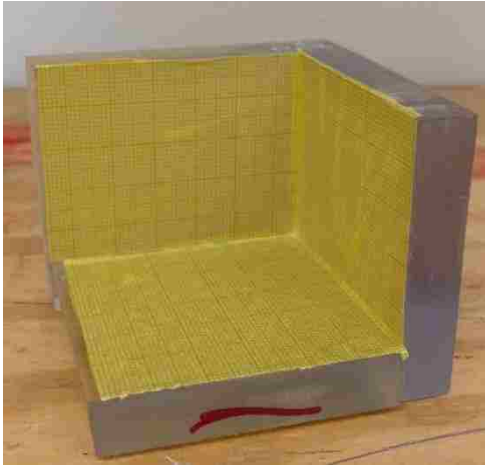mark where to stop timing. The testing column can be seen in Figure 19.

Figure 18: Fiber Measuring Station

Figure 19: Still Water Column

4.3   Procedures

The fiber clusters used for testing were prepared using the modified NEI method [3,4]. The method used a pressure washer and bucket as a means to break large sheets of NUKON into smaller clusters. Once the fiber was prepared, it was strained and stored in Nalgene bottles for later use. A more complete description of the preparation method is provided in the references [3,4]. A brief summary of the preparation procedure is given below.

A square of fiber was first cut from the larger sheet using a pair of scissors (Figure 20a). The sheet was then separated into 8-10 layers, and placed in a 5-gallon bucket with about an inch of water already at the bottom (Figure 20b and 20c). An 1800 psi pressure washer with a 40° fan type nozzle was used to break the fiber into small clusters (Figure 20d). This was done by placing the tip of nozzle 1 inch below the surface of the water, and moving the tip around the bucket. The fiber was then strained using a 40-micron mesh sieve (Figure 20e). Strained fiber was placed in either a 1-liter Nalgene bottle with sufficient water for storage, or it was transferred into a 2L beaker with water to be further processed.

The fiber that would be further processed was placed into the 2L beaker with a large stir bar at the bottom (Figure 21b), and then onto a stir plate. The stir plate was turned on to the highest possible setting, and the fiber was also broken up manually by hand with a stir rod at the same time as it was being agitated by the stir bar (Figure 21d). Once samples had been stirred, the fiber was transferred into 1L Nalgene bottles for storage. Fiber clusters had two designations, processed and unprocessed. The processed fiber was representative of new preparation techniques [3,4], and lead to clusters of smaller average size. The unprocessed fiber was similar to older preparation techniques [8], and lead to larger cluster size.

Figure 20: Fiber Preparation Procedure
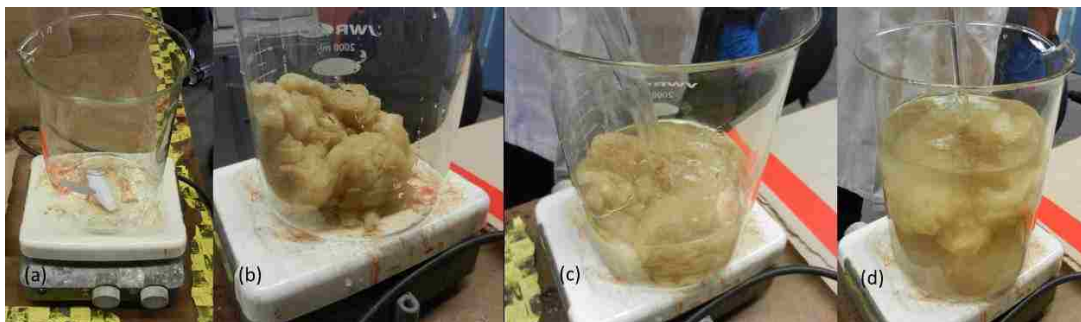
Figure 21: Post Processing Procedure

After the fiber was prepared, individual samples were labeled and measured. The fiber samples were labeled using a naming scheme where the test series is denoted by a letter and the sample denoted with a number. Individual fiber clusters were "plucked" from the batch using a pair of stainless steel tweezers. They were then submerged into a beaker of DI water and gently shaken to remove any loose fines that might be clinging to the cluster. Once fines were shaken off of the sample, the sample was placed onto the measuring station. A lint free tissue was used to remove any excess water that might distort the photo. Pictures were taken of the top, left, and right sides the sample. Pictures of the submersion can be seen in Figures 22 and 23.

Figure 22: Fiber Cluster Before DI Rinse

Figure 23: Fiber Cluster After DI Rinse

Along with drop tests done in tap water, a series of tests were run with a 50/50 volume ratio water and glycerin. This was done to alter the Reynolds number of the sample and help fill in the data in the lower reynolds range (10-50). Tests were done in the exact same manner as before except the liquid in the test column was replaced with the mixture. The liquid used to store and rinse the fiber clusters was also replaced with the water glycerin mixture.

The area, perimeter, and height measurements were all analyzed with the aid of PowerPoint. The "top" picture and one "side" picture for each sample were loaded onto individual slides. It was at this time that a choice of which side picture better depicts the average heights was chosen. In practice it was typically the photo that depicted the larger side of the sample (IE the picture where the sample takes up more grid squares).
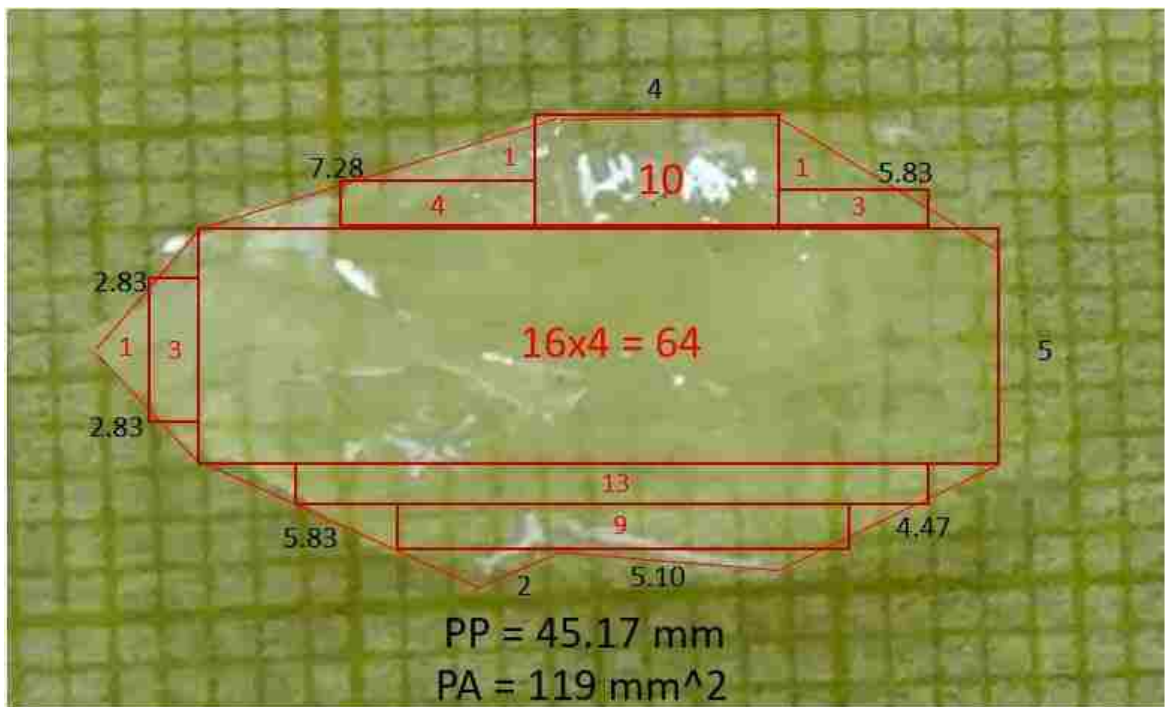

Figure 24: Projected Perimeter and Projected Area Measurements

The first measurement that was taken after the samples have been photographed was the projected perimeter. This was done by encircling the sample with connecting straight lines that best

match the samples edges. These lines were then measured by counting the grid squares they cover. For lines that were not parallel to either grid axis, Pythagorean's theorem was used to best estimate their length. An examples of a projected perimeter calculation can be seen in Figure 24, with the numbers in black representing line segment lengths.

The second measurement that was performed was the projected area of the sample. This was done using the rectangle tool within PowerPoint. Rectangles were drawn onto the sample picture such that their areas are fully, or close to fully enclosed by the sample. Once the sample had been completely covered in rectangles, the area of each rectangle was estimated by counting grid squares along the length and width of the rectangle. The sum of all the areas of all the rectangles was used as the projected area estimate for that given sample. An example of the projected area calculation can be seen in Figure 24, where the red numbers indicate rectangle areas, and the estimated projected area can be seen at the bottom of the figure in black. It should be noted that projected area estimates made using this procedure tend to be underestimated. Underestimated samples were preferred to overestimate samples because the fibers near the edges of the clusters were not as closely packed as the fibers near the center of the samples. It was thought that this underestimation would lead to more accurate results when used in conjunction with the assumption that the clusters retain the same porosity after preparation that they had when packaged.

Figure 25: average height measurement

The final measurement taken of the fiber clusters was the average height. This measurement was made using the "side" picture of the sample. The sample was first outlined using straight red lines, this can be seen in Figure 25. The height of the sample was estimated over the distance of one grid square. This process was repeated for each grid square the sample takes up, and the values were summed and averaged.

After the clusters had been rinsed and measured, they were used in a single settling test. Fibers were picked up from the measuring station using a pair of stainless steel tweezers. The sample was then taken to the column where it would be tested. A stopwatch was readied by clearing the previous time from the screen. The fiber cluster was then placed just under the surface of the water using the tweezers. Care was taken to ensure that the fiber cluster had its minor axis aligned with the fall direction. This was done to prevent tumbling and twisting, which could lead to erroneous data.

Once the cluster had fallen for 30 cm, measured by a line on the side of the column, the stopwatch was started. The time that it took the cluster to fall the remaining 100 cm was recorded and written down in the lab notebook. This was the time that was used to calculate the clusters terminal velocity. During the test, clusters must be constantly observed to check for criteria that could deem the test data unusable. If the fiber cluster was settling to close to the wall (around 1 to 2 cm) or touched the wall a note was made so that the data for that sample could be thrown out. Also, if the cluster started to tumble, or had a spurt of sudden acceleration the data was thrown out. The last reason for deeming a sample unusable is if any part of the cluster breaks apart. Projected area and perimeter are meaningful measurements to the development of the correlation, so if the integrity of the sample was compromised in any way the data was deemed unusable. After a sample has finished settling, the column was allowed to stagnate for around 2 minutes and then the process was repeated.

A series of dye tests were also run in the settling column. The first of those tests was run using the same mixture of water and glycerin that was used to fill in values for low Reynolds settling. The latter tests were run using tap water. Regardless of the medium, the sample preparation and testing procedure was the same. Samples were selected and measured in the same was as was done for the settling tests. After pictures were taken of the samples, blue food coloring was dropped onto the sample until it was completely saturated. The sample was then dropped in the column and timed as normal, the only difference being that these tests were recorded with a video camera such that still images of the dye trails could be used for wake analysis.

4.4   Uncertainty Analysis

Any instrument used in scientific testing has a quantifiable uncertainty associated with it. Along with quantifiable uncertainty, the experiments run for this thesis have several sources of error from assumptions that cannot be measured. Of the errors that can be measured there are two types, random and systematic. For this experiment, the random errors are the ones that arose when measuring the fall time and when measuring the size of the particles. They come from the human factor involved in stopping the stop watch accurately, and estimating the sizes of fiberglass samples. These measurements could not be repeated because fiber samples cannot be reused in multiple tests. These types of errors effect different samples to different degrees. For example, the stop watch error effects faster falling samples more than slower ones. This is because the error associated with stopping the stop watch is the same regardless of how long the sample takes to fall, and the percentage error for faster samples is higher than that of slower samples. The random errors associated with this experiment are listed in the table seen in Figure 26.

Random Errors		
instrument	uncertainty	uses
stop watch	± 0.28 s	velocity
area grid	± 1 mm²	projected area
length grid	± 0.5 mm	projected perimeter
height grid	± 0.5 mm	average height

Figure 26: Random Errors Associated with Settling Tests and Fiber Measurement

The second type of errors that arise in experimentation are labeled systematic errors. These are errors that are associated with specific instruments that are used to measure the physical properties of the liquids used for testing. These errors are the same for all the samples that were tested, because the same instruments in the same fashion were used for all of the tests. Systematic errors can effect measurements in two ways, offset error and scale factor error. Systematic errors are difficult to detect and affect all samples in the same way, for this reason they are left out of the uncertainty analysis used to calculate the error bars seen in the Results section. The sources of systematic error and their error values can be seen in Figure 27.

Systematic Errors		
instrument	uncertainty	uses
tape measure	± 2 mm	velocity
thermometer	± 0.2°C	viscosity/density
viscometer	0.16%	viscosity
volumetric flask	± 0.2mL	density

Figure 27: Systematic Errors Associated with Settling Tests

After fall data was collected an uncertainty analysis was performed using the values in Figure 26. Error was propagated through equations 10 and 11 for the Reynolds number, and equation 23 for the measured drag coefficient.

Chapter 5 Results

5.1   Introduction

Four series of tests were run in order to collect data in different Reynolds ranges. These tests were labeled A through D where A was a shakedown series, B was a series using fiber that was not post processed, C was a series using post processed fiber, and D was a series using both fiber preparation methods, and the tests were performed in a 50/50 volume mixture of water and glycerin. In the following results section only data from the B, C and D series is shown as the images from the A series were difficult to analyze. This shakedown series was important to work out the procedures that would be used for the rest of the series that were performed. The B series tests used the largest of the fiber clusters, with Reynolds numbers ranging from 47 to 350 and characteristic length values from 5 to 13 mm. After the B series of tests were run, it was believed that running samples that had been post processed would lead to lower Reynolds numbers and thus help to "fill in" the range of the samples. The C series samples had a Reynolds range from 84 to 283 and characteristic lengths from 4 to 7 mm. Samples in the C series tests were smaller in L range, they tended to be rounder (kernel-like), fell faster, and still had high Reynolds numbers. After the post processed fiber still led to Reynolds numbers above 50, it was decided to change the liquid used for tests in order to lower the Reynolds numbers of samples. This was done by filling the column with a mixture of 50% water and 50% vegetable glycerin by volume. This changed the viscosity of the liquid in the column from around 1 centipoise to around 6 centipoise and drove the Reynolds number of the samples down to below 40.

The object of the series of drop tests was to compare the data collected for fiber clusters with a known correlation for sand grains. This was done by calculating the Reynolds number and drag coefficient for each sample that was used in a drop test. As discussed previously in chapter 3, the Reynolds number was calculated using a weighted ratio of projected area to projected perimeter, along with viscosity, and velocity measurements. Velocity was measured using a stop watch, while the viscosity was either looked up in a table for pure water, or measured using a viscometer for the mixture.

Along with settling tests, a series of flow visualization tests were run in order to better understand the wake behavior for fiber clusters. These flow visualization tests were labeled the DYE series of tests, and were preformed both in pure water, and in the water/glycerin mixture. Results from the DYE series of tests are compared to the results from Willmarth et al. on the wake behavior of disks [15].

5.2   Quantitative Results

The data collected for the drag coefficient and Reynolds number of the fiber clusters behave similar to the prediction made in chapter 3. Samples with Reynolds numbers below 100 mirror the behavior of stokes law and have drag coefficients that are inversely proportional to the Reynolds number. While samples with Reynolds numbers above 100 approach a constant limiting value. These two behaviors are the driving phenomenology behind the Cheng correlation (equation 14). The two behaviors can be seen in Figure 28 with the D series samples and some of the low Reynolds B series samples exhibiting stokes behavior, and the C series samples and remainder of the B series samples exhibiting drag limiting behavior.
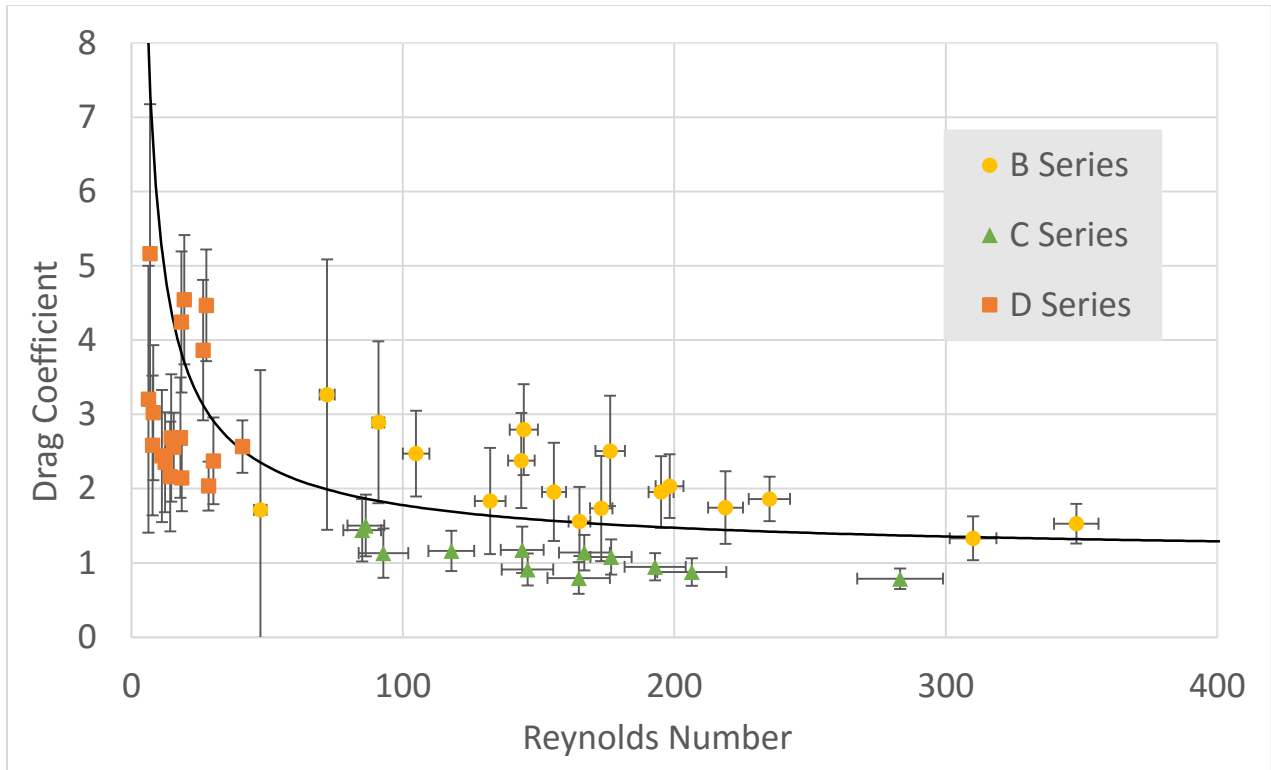
Figure 28: Reynolds number vs Drag Coefficient

When the correlation developed by Cheng is overlaid onto the Reynolds vs drag plot for the terminal settling velocity tests, it is seen that the data for NUKON clusters follows a similar trend. There is some interesting behavior of fiber clusters when you look at the series individually. The Cheng correlation tends to under predict the drag coefficient for B series, and over predict the coefficient for the C series. It is possible that this is due to the preparation difference between the two series. The C series samples were post processed, leading to fiber clusters that were smaller and with a more kernel like appearance. This can be seen numerically in Figures 29 and 31. The average characteristic length for the C series is 5.8mm while for the B series it is 9.8mm. An example of a C series cluster can be seen in Figure 28. The smaller kernel-like particles behave more like ellipsoids than flat disks, and thus the measured drag coefficient for the flatter B series particles is higher than for the C series.

series	B	C	D
Re mean	171	155	19
(min-max)	(47-348)	(85-283)	(5-41)
L mean	9.8	5.8	10.1
(min-max)	(5.3-13.9)	(4.2-8.0)	(5.2-15.7)
Cd mean	2.1	1.1	3.3
(min-max)	(1.3-3.3)	(0.8-1.5)	(2.1-5.2)

Figure 29: Series Reynolds, Characteristic Lengths, and Drag Coefficient Data

Figure 30: C Series Sample

The samples that made up the majority of the C series were from the unbaked portion of the NUKON sheet. This statement can be made based upon the characteristics of the clusters. They hold their shape much better that cluster from the other series, they are more yellow, and denser. All of which are characteristics of the unbaked portions of the NUKON sheets. This can be seen visually by comparing the C series cluster in Figure 30 to a B series cluster seen in Figure 32. The C series sample is

49

more yellow, and less opaque than the B series sample. The post processing procedure broke C series

samples into very small pieces and the projected areas of the C series samples were the smallest of any

series with an average of 35mm^2. However, the excess binder that is present in the unbaked portion of

the NUKON also led to samples with large average height. Smaller than average projected area, and

larger than normal average height lead to samples that were the most sphere like out of all the series.

This can be seen numerically later in the chapter when the CSF is used as a shape measurement.

This is evidence that one of the assumptions made in chapter 3 is invalid. It is assumed that

the fiber clusters retain their as fabricated porosity (Figure 16), however from inspection this

assumption is false. The extent that this assumption is false is yet to be quantified, and it is unclear

whether or not this has something to do with the NUKON sheets being partially baked. The values given

in Figure 16 are based on factory sheets of NUKON, and do not account for the baking process.

series	B	C	D
Area Mean (min-max)	112.8 (40-219)	35.2 (18-59)	101 (24-259)
Perimeter Mean (min-max)	44.6 (27.7-63)	23.7 (17.0-35.3)	38.6 (18.5-66.0)
Height Mean (min-max)	1.9 (0.5-3.4)	2.3 (1.8-3.3)	2.1 (0.9-3.9)

Figure 31: Series Projected Area, Projected Perimeter, and Average Height Data

The combination of the C series samples being more ellipsoidal than disk shaped, and being

denser lead to particles that fell faster than expected. Faster falling particles also means higher Reynolds

numbers than expected with less drag. The clusters in the B series tests were polar opposite to the C

series. The clusters had larger projected areas, and had average height values smaller than the C series

samples. With the large projected areas and smaller height values, the B series samples resemble

amorphous thin disks, and were either predicted accurately or slightly under predicted by Cheng's

correlation. A cluster from the B series samples can be seen in Figure 32, noting the larger encompassed area and less yellow color.

Figure 32: B Series Sample

Three outliers were thrown out of the B series samples. They all had recorded drag values that were much higher than the values predicted by Cheng's Correlation. Notes taken about the fall of each of those samples reveal abnormalities, or spirals during testing.   It is concluded that either wall effects, or effects from the water in the column (not being perfectly still) adversely affected the samples causing erroneously high drag values.

Based on the observations on the size and shape of the B and C series tests and on the error bars in Figure 28, it is clear that the random errors affect the three series differently. The B and D series samples, which were large flat samples with slow velocities have large drag uncertainty and small

Reynolds uncertainty, while` the C series samples which were small ellipsoidal samples have large

Reynolds uncertainty and small drag uncertainty. This is partly due to the different sizes of the particles,

and partly due to their terminal velocity. The drag coefficient is most affected by the uncertainty due to

average height measurement, and the uncertainty due to velocity measurement. The uncertainty effects

smaller height measurements and faster velocity measurements more than it affects large heights and

slower velocities respectively. This leads to the small drag uncertainty for the C series samples and for all

but three of the B series samples. The 3 outlying B series samples, from left to right in Figure 1, have

average height values of 0.46mm, 0.91mm, and 1.36mm. It is for this reason that the error bars

associated with them are so long in the drag direction. Similarly, the error bars associated with both high

Reynolds B series samples and most of the C series samples have high Reynolds uncertainty due to their

relatively faster fall velocities.

The D series samples were run using a mixture of half glycerin half water by volume. The idea

behind this series was to generate samples in the lower Reynolds range (5-50). Testing samples with

areas smaller than around five square millimeters proved very difficult. It was decided to drop the

Reynolds range by changing the fluid instead of trying to analyze smaller samples. The results for the D

series samples were mixed. Five of the samples land near the Cheng correlation, but the other 13

samples are all clustered around the same point in the graph well below and to the left of the Cheng

correlation. The error associated with the D series is also similar to that associated with the B series. All

save a few of the D series samples were large and flat, with low velocities (due to the highly viscous

liquid). This leads to relatively large drag errors with small Reynolds error.

The discrepancies in the D series tests can be more easily seen in Figure 31. The graph shows

measured vs predicted drag coefficients for the A, B, and C series samples. Five lines are overlaid onto

the plot which represent perfectly predicted (solid), plus or minus 10% (large dash), and plus or minus

20% (dot dash). Most of the samples from the B and C series tests fall in the plus or minus 10% range

with a few from the B series going just over that. The D series tests have samples ranging anywhere

from right on the match line, all the way to well outside of the plus 20% line.

Along with the D series discrepancies, the actual vs predicted plot clearly shows that the Cheng

correlation is under predicting the B series samples, and over predicting the C series samples. This was

seen earlier in Figure 28, and with the error bars and prediction lines present it is shown that the under

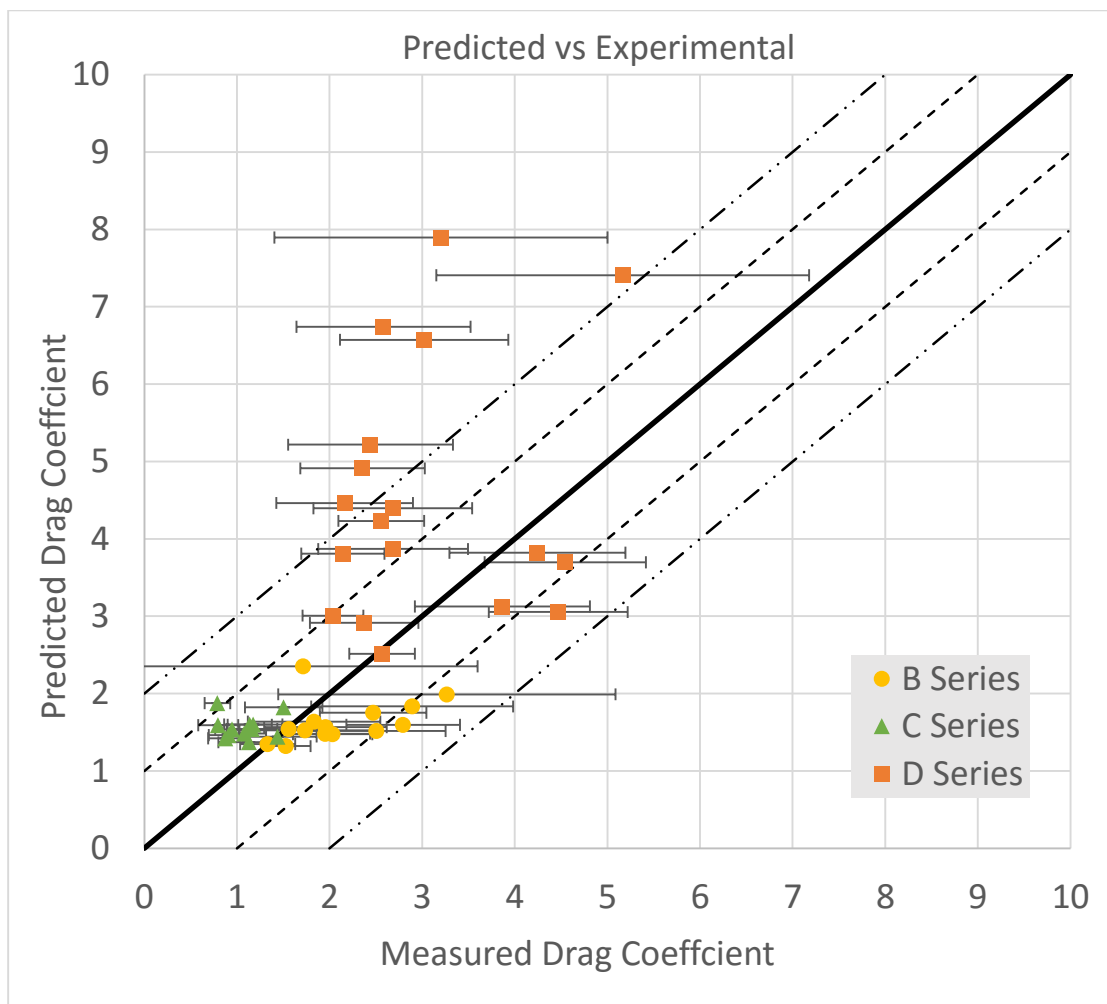and over predictions do not vary by more than 10% in most cases.

Figure 33: Measured Drag Coefficient vs Predicted Drag Coefficient

From the current analysis it is clear, there is some discrepancy when it comes to the prediction

of the drag coefficient for fiber clusters. The only reason that this might be occurring is relative size, and

relative shape of the particles (disk vs ellipsoid), however that reason only applies to the B and C series. All of the D series samples where from the same batch of fiber, and all of them were from a batch that was not post processed. There were some clusters that had a "kernel" shape, but not nearly what was present in the C series tests.

Plots of all kinds were generated in order to see if trends occurred with variables that are not taken into consideration by the Cheng correlation. The use of the Corey shape factor (CSF) was utilized as a means to better understand the discrepancies within the sets of data, and lead to some meaningful results. The CSF is a measure of the flatness of a particle, C series samples would have values closer to unity than those in the B or D series. The equation for the CSF was presented in Chapter three equation 12. In order to use the CSF, measurements of the major, minor, and intermediate axes had to be made. These measurements were made using the existing photographs taken of the samples for size measurement.

The first trend that was noticed was a negative exponential trend with drag coefficient and velocity. The plot can be seen in Figure 34 and a log-log version in Figure 35. An interesting pattern forms when the velocity is in place of the Reynolds number. The series start to differentiate themselves based on terminal velocity. The "kernel" shaped pieces all had higher than average velocity values, due to their rounder shape. This lead to them having lower drag coefficients than the rest of the tested samples. This is seen clearly in Figure 28 with most of the C series data falling under the Cheng correlation, however in the velocity plot the data ends at the far right, but follows the same trend as the other two series. The addition of a length component in the Reynolds number makes the differences in the two series more obvious.

A conclusion can thus be made that either the density differences between the two different types of samples was making the measured drag readings erroneous, or the way that Reynolds number is calculated for the current samples is not realistic for smaller samples that resemble ellipsoids.
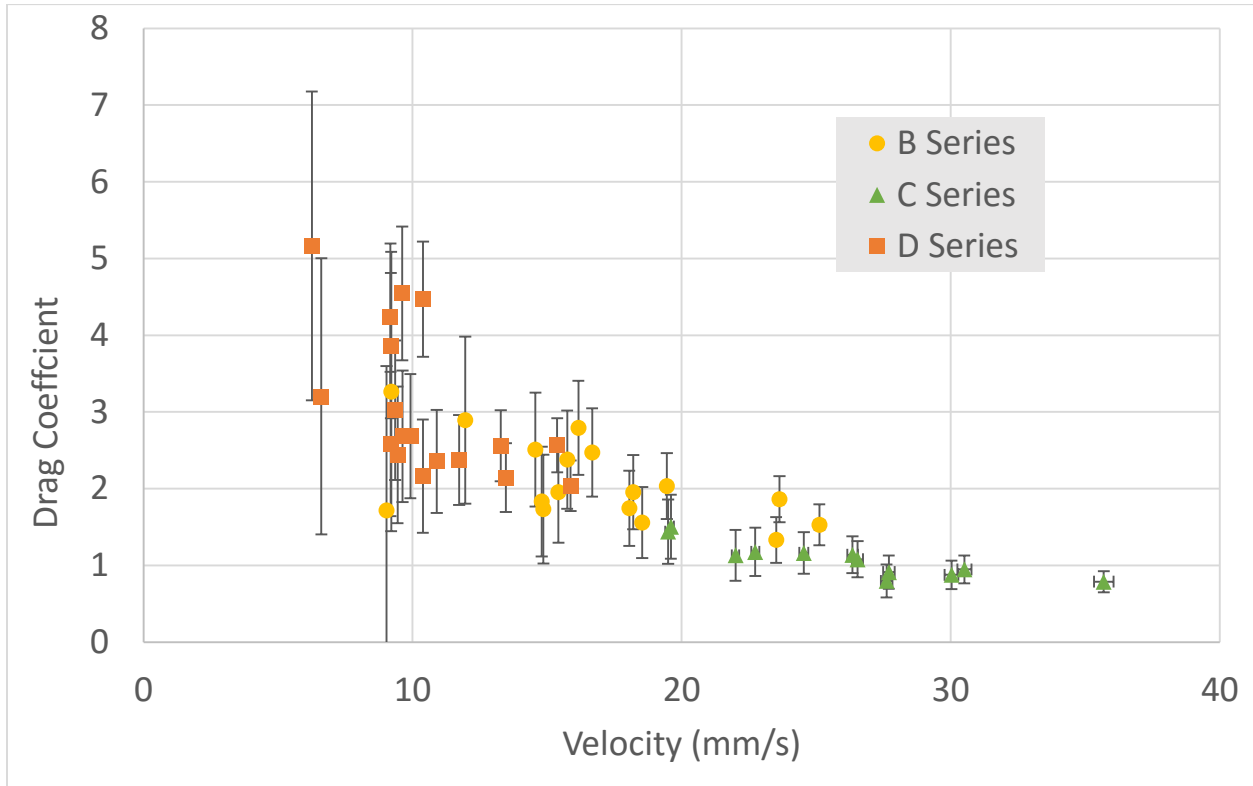

Figure 34: Velocity vs Drag Coefficient

The B and D series follow the same trend as the C series discussed above. All three of the data sets overlap at the ends of their respective velocity scales, but the drag coefficient matches well for these overlaps, where as in the Drag vs Reynolds plot the gaps between the three series are more pronounced. This could be used as an argument against the densities being a reason for discrepancies seen in Figure 28.

The CSF was used to try and understand the discrepancies that arose between the B and C series tests. It was not used on the D series test, because it has no way to take into account the effects of viscosity, thus the comparison would not have been useful. The first plot can be seen in Figure 35 and

correlates the CSF with the drag coefficient. A negative linear trend can be seen from this plot, which makes sense from a physical standpoint. The higher the CSF the closer the particle is to resembling a perfectly isometric particle (such as a sphere or cube), the lower the drag coefficient. Perfectly isometric particles tend to have drag coefficients that are lower for a given velocity than particles that are less isometric (disks, sand, etc.). The plot also shows that the C series samples have higher CSF's (rounder) corresponding to lower drag coefficients. This was speculated earlier, and is confirmed with the CSF.
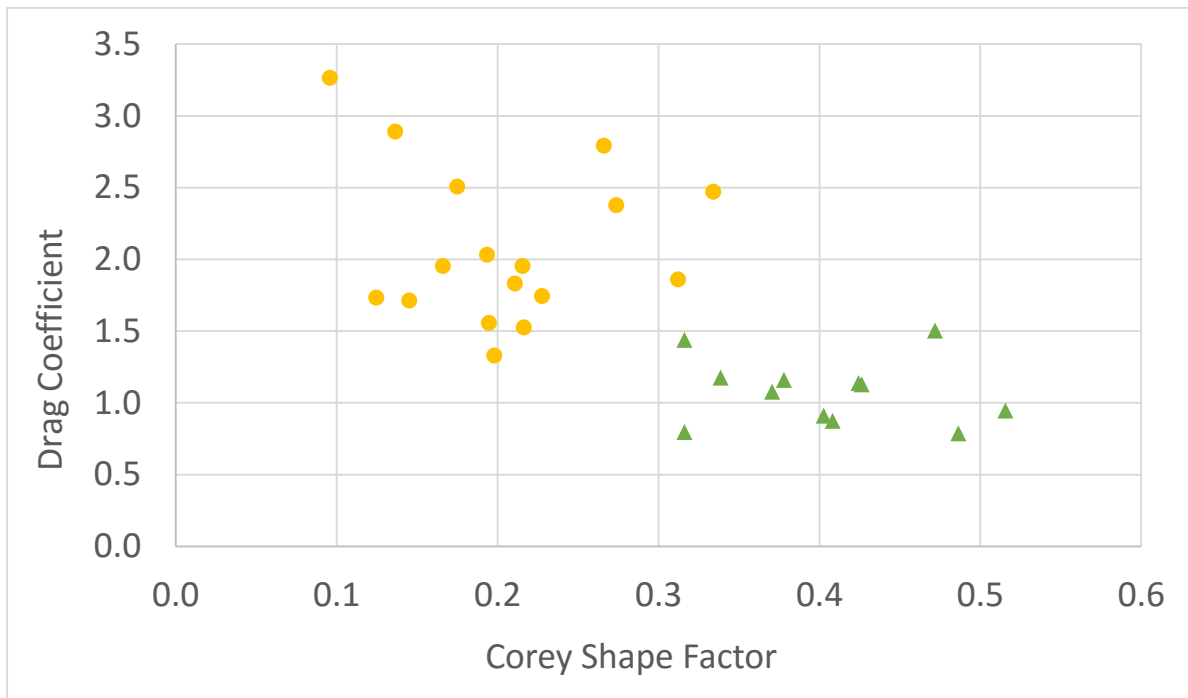

Figure 35: CSF vs Drag Coefficient

Velocity is another term that is highly dependent on shape. The flatter the object, the more drag it has and thus the slower its terminal velocity will be. Figure 36 presents a graph of CSF on the x axis with velocity on the y axis. A clear positive linear trend is formed as the particles that are less flat fall faster than the flatter ones. As before there is a clear distinction between the B and C series tests, and it can be seen that the average velocity of a C series particle is higher than that of its B series counterpart. From Figure 34 it was shown that the drag coefficient is inversely proportional to the velocity, and now

it is seen that the velocity is directly proportional the CSF. This is more evidence that the differences in shape between the series is leading to faster terminal velocities for thee C series samples and thus lower drag coefficients that predicted of the C series.

A conclusion that can be drawn from the CSF plots, is that the particle shape is making a direct impact on velocity and subsequently the drag of the particles. This impact is not fully taken into account either by the Cheng correlation, or by the Reynolds number calculation used in Figure 28. It is most likely an issue with the Reynolds number calculation, or more specifically the characteristic length. Comparing Figure 28 to Figure 34, the x values of the plot differ only in that the Reynolds number takes into account length and viscosity. Looking only at the values for B and C series samples, the viscosity is the same, and the only difference is then the length. Equation 11 used for the characteristic length for the particles does not depend on the average height of the particle. This is perhaps one of the reasons that the B and C series diverge from each other and fall on opposite sides of the Cheng correlation.
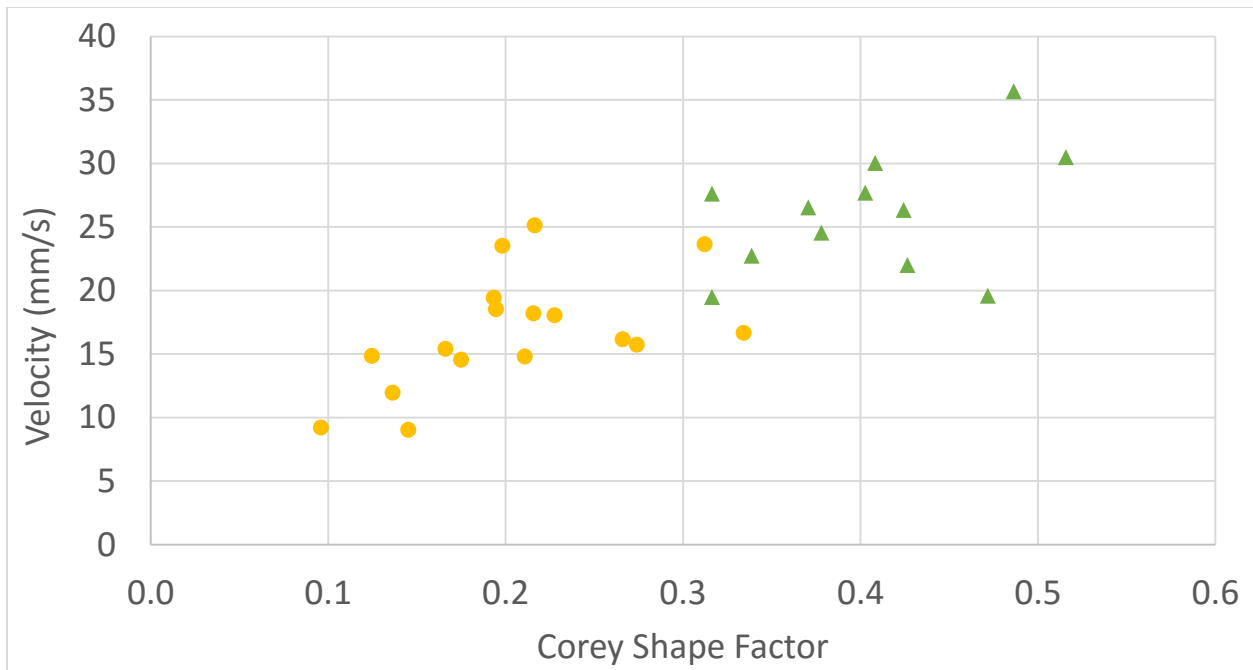

Figure 36: CSF vs Velocity

5.3   Qualitative Results

In order to better understand the differences between the three main series of tests, dyed samples were run and photos were taken as a means of flow visualization. This also allowed for the fiber samples of this work to be compared with the dye tests run by Willmarth et al. [15] on thin discs. The dye trails that are left behind can give insight into the flow regime, and allow for a better understanding of how the clusters oscillate as they fall.

The dye tests were run on samples that were representative of the three main series of tests run for this research. Tests were run in a water glycerin mixture, tests were run with large flat samples, and tests were run with compact "kernel-like" samples. A wide range of Reynolds numbers were run as to visualize the differences between slow and fast falling samples, as well as small and large samples. Videos were taken and still images were pulled from the videos for comparison. The samples were labeled DYE 01 through DYE 06. The Reynolds numbers that were measured for the sample try and follow an increasing trend, but are jumpy because it is difficult to predict what the exact Reynolds value will be before the test takes place.

The glycerin mixture tests were the first to be run, as the column was still filled with glycerin from the D series tests. Three tests were run with the first of the tests giving the best visual results, and being the only one included as results. The sample is labeled DYE 01, and can be seen in Figure 36a through 36d. The pictures depict a sample with an approximate Reynolds number of six. At Reynolds numbers this low the flow is clearly laminar. The dye trails in all four figures show smooth straight lines that are parallel to the flow direction, and no swirling or vortices are present in the wake. In a similar fashion to the disks that were tested by Willmarth et al. [15] the sample "righted" itself such that the largest area was perpendicular to the flow direction, however this took noticeably longer than the samples in water (higher Re). While the clusters do behave similar to disks and spheres at similar

58

Reynolds numbers, there are some key differences. The number or dye trails leaving the sample starts at about three and reaches around four or five by the time the sample disappears from view. Both disks and spheres only leave behind a single trail at Reynolds numbers this low. This is most likely due to the irregular nature of the fiber clusters. The edges of the clusters are jagged and thus prevent the flow field from reforming along the back of the sample. This creates the many distinct dye trails that can are seen in Figure 37.
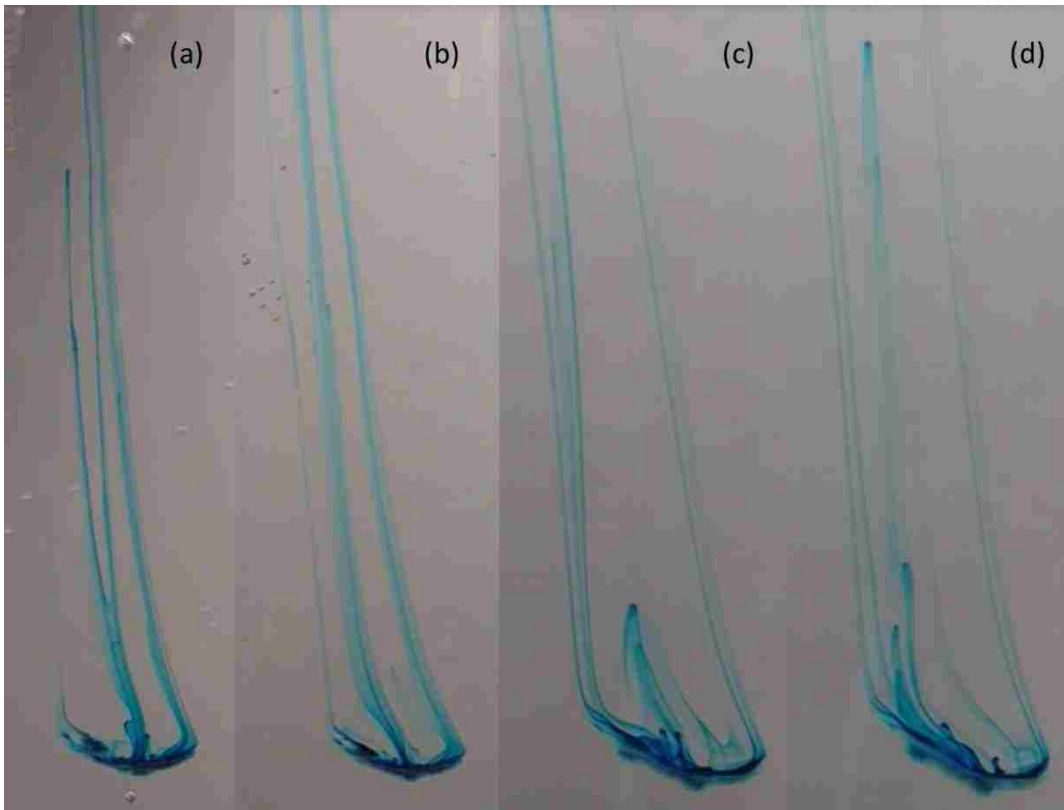

Figure 37: DYE 01 (Re≈6)

DYE 02 was a small sample that was run with the column filled with water, and a Reynolds number of around 55. An interesting phenomena appears in the dye trails of this sample and all other samples that had Reynolds numbers higher than 55. Irregularly shaped vortices are shed off of opposing sides of the particle. These vortices are caused by the sample oscillating back and forth along its intermediate axis. One vortex is formed every time the particle wobbles to the side, and thus they

alternate on either side of the particle. The particle wobble is seen when comparing the orientation of

the sample itself in Figure 37a and 37b, in 37a the cluster face is completely perpendicular to the flow

and in 37b it is at a slight angle.

Figure 38: DYE 02 (Re≈55)

DYE 03 was similar in size to DYE 02 and had a Reynolds number of around 74. This sample showed similar oscillations, however they were larger in amplitude with similar frequency. The same vortex shedding that was seen in the previous sample was also seen in this sample. The vortex rings that were shed resembled a horseshoe in shape. Similar horseshoe shaped rings were seen by Willmarth et al. in their work with thin disks. The vortices can clearly be seen in the top of Figure 39a and the bottom of Figure 39b near the sample. The vortices shed by DYE 02 were also horseshoe shaped, but were less pronounced than those seen in DYE 03.

Figure 39: DYE 03 (Re≈74)

So far the three samples that have been dye tested have been representative of the D and B series. DYE 01 was of similar Reynolds numbers as D series samples, and DYE 02 and 03 had similar Reynolds numbers, and similar shape to some of the B series samples. In order to better understand the differences that arose in the three series of tests, samples similar to the C series were dye tested next. These samples were picked from post processed fiberglass and had a similar "kernel" shape.

DYE 04 was he first "kernel" sample that was run, and had a Reynolds number of about 200. The sample exhibited similar behavior to the other dye tests that were in water. This sample confirmed the previous observation that the samples tend to "wobble" about their intermediate axis. The video of this particular sample was taken such that half of it was shot from the side, and the other half was shot facing the column straight on. In Figure 40a and 40b the intermediate axis is projected in the picture, the dye trails in these pictures show small oscillations. In Figure 40c the camera has moved such that the intermediate axis is pointing towards the viewer. The dye trail oscillations in this image have a greater amplitude than the ones in Figure 40a and 40b. The increased Reynolds number also leads to larger amplitude oscillations when compared to the oscillations at lower Reynolds numbers (Figure 38a through 39b). The vortices that are shed at this higher Reynolds number are also less stable and show more dissipation than the vortices that were shed at lower Reynolds numbers.
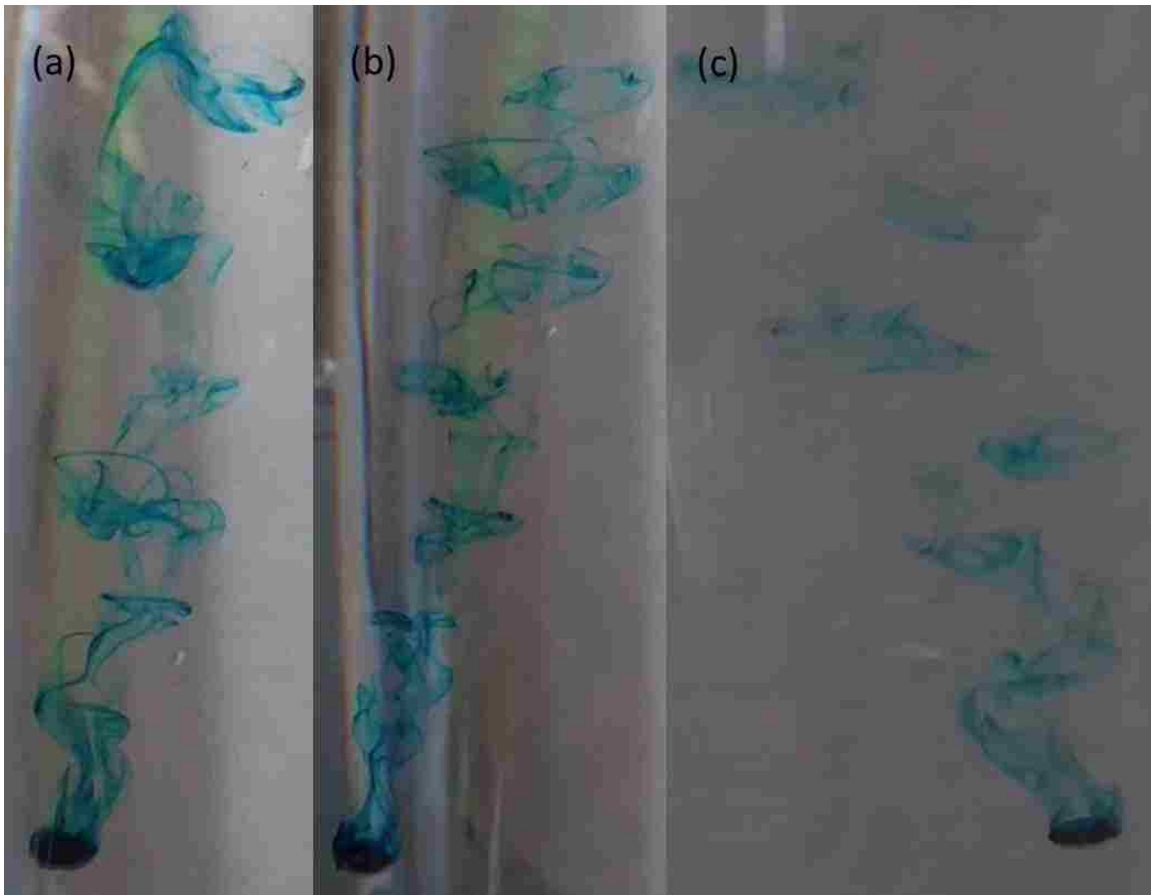
Figure 40: DYE 04 (Re≈200)

As the Reynolds number for the dye tests is increased, the same vortices and dissipation is seen in the dye trails. The final two dye tests that were run had Reynolds numbers of around 240 and 480 respectively. Small vortices stemming from the particle oscillation can be seen in Figures 41a through 41c, and the dissipation of said vortices due to the higher Reynolds numbers of theses samples can be seen most clearly in Figure 41c and 42a near the top of those images.
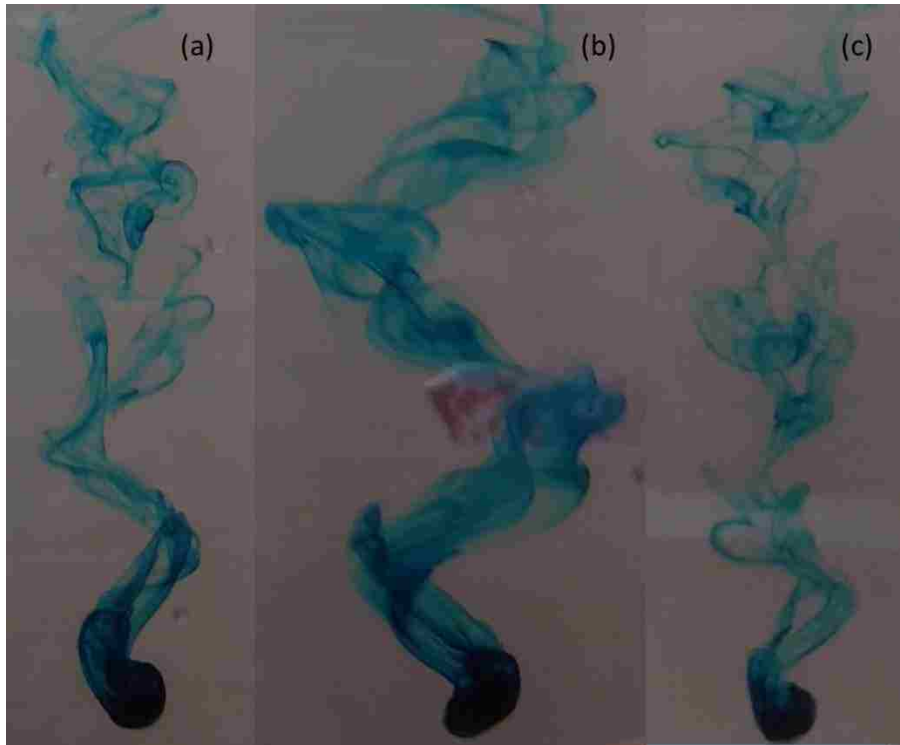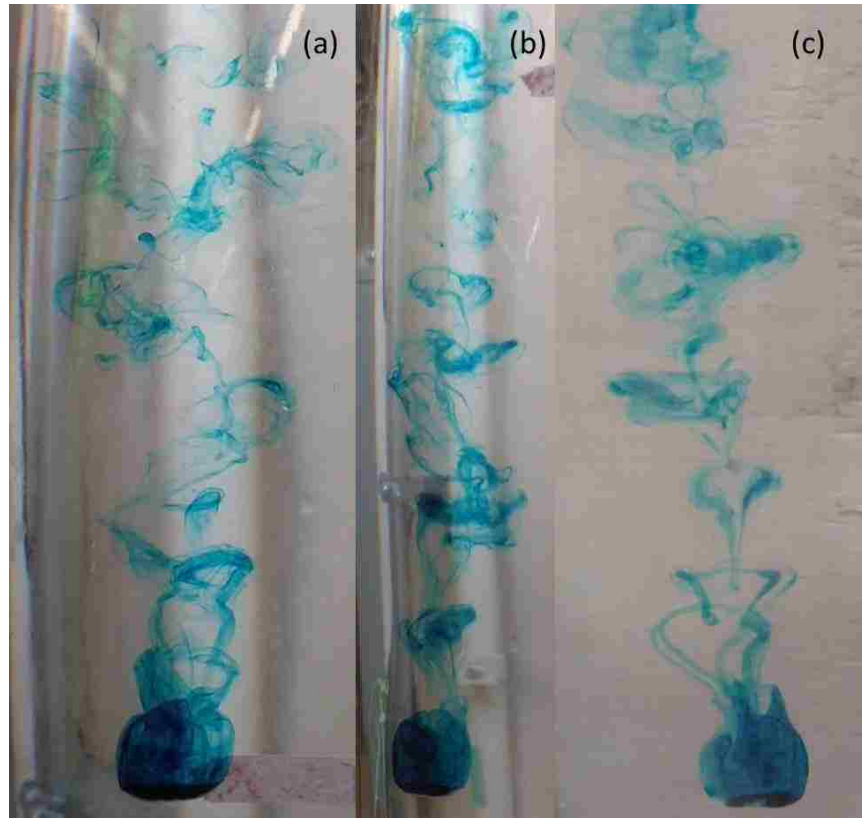
Figure 41: DYE 05 (Re≈240)

Figure 42: DYE 06 (Re≈480)

The oscillations that were seen in the dye tests that were completed in water, are reminiscent of the oscillations observed by Willmarth et al. in their study of thin disks [15]. They observed oscillations in disks above a Reynolds number of 100. These oscillations were labeled one of three types: stable, unstable, or boundary. Unstable disks were ones where the amplitude of their oscillation increased, stable disks had no oscillations or had oscillations that were damped, and boundary disks had no change in the amplitude of their oscillations [15].

The dye trails that were observed by Willmarth for unstable, and boundary disks mimic the dye trails that are seen for the water dye tests run on fiberglass clusters. Of the five samples that were run in water, the ones under a Reynolds number of 100 were observed to be damped, and the ones above Reynolds number of 100 were undamped or of boundary motion. The sample that had a Reynolds

number of around 480 exhibited little oscillatory motion. This is because the sample was sufficiently

large. Willmarth et al. noted that disks with large values for moment of Inertia behaved as fixed disks

during settling [15], and it is believed that this fiber sample is behaving similarly. The summary of

stability data can be seen in the table in Figure 43.

The dye trails for the undamped motion of the disks tested by Willmarth mirror the trails from

Figure 40 when looked at normal to the oscillatory motion, and then again with the camera turned 90°.

The images of the oscillatory motion of this specific thin disk can be seen in Figure 44a and 44b.

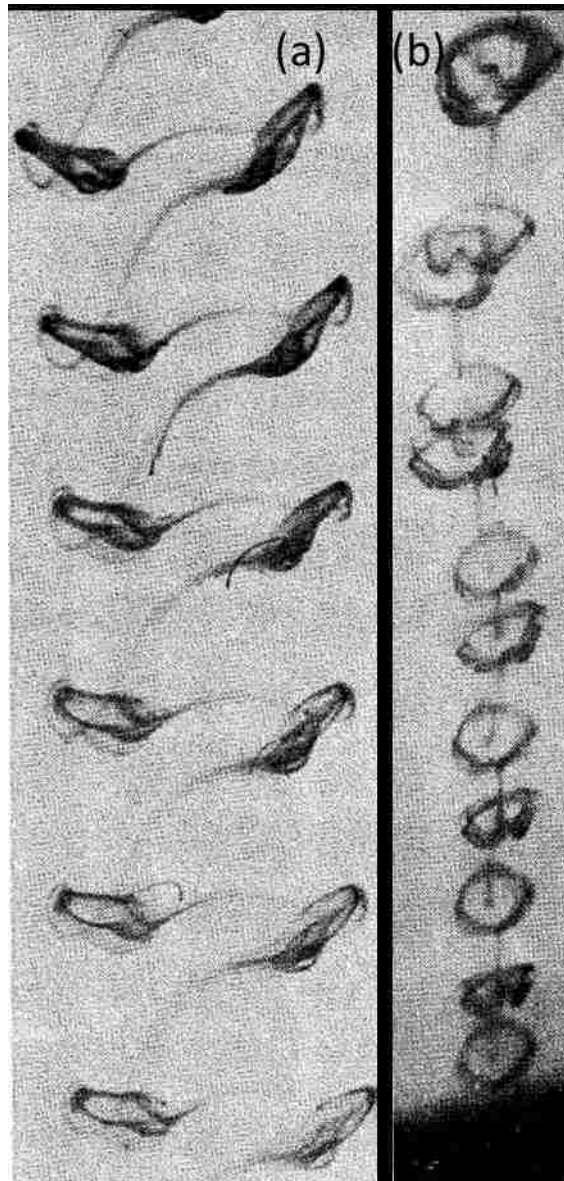| DYE Series Samples			
sample	medium	Re	osscilation
DYE 01	mixture	6	none
DYE 02	water	55	damped
DYE 03	water	74	damped
DYE 04	water	200	undamped
DYE 05	water	240	undamped
DYE 06	water	480	none

Figure 43: DYE Series Stability Data

Figure 44: Oscillatory Motion of Thin Disk Viewed Normal to Oscillation (a) and 90° from Normal (b) Re=170 [15]

Willmarth et al. utilized three dimensionless numbers to characterize the oscillatory motion of free falling disks. They are the Reynolds number, the thickness ratio, and the dimensionless moment of inertia. They note that the thickness ratio has an impact on the dimensionless moment of inertia, and thus the pitching motion of the disks [15]. They also state that if the thickness ratio is small enough the effects that it has on samples with differing thickness ratios is negligible [15]. This is where the comparison to fiber clusters starts to fall apart. The thickness ratio of an average cluster is much larger

68

than the thickness ratios of Willmarth's disks all of which have thickness ratios less than 0.04 [15]. Along with the thickness ratios being larger for clusters than for disks, it is nearly impossible to accurately measure the moment of inertia and thus derive the dimensionless moment of inertia for clusters. This makes it difficult to compare the stability characteristics of the fiberglass clusters. This being said, the qualitative characteristics of the wakes of both types of particles can still be compared, and the stability information can still be measured in terms of Reynolds numbers.

Willmarth et al. made two observations about unstable disk motion that are directly comparable to the settling of clusters. The first is that the pitching motion of the disks was followed by a large amplitude translation of the disk through a plane normal to the pitching motion [15]. This same pitching followed by translation was observed for all the dye samples that were tested in water, even the samples whose oscillation was dampening. These translations are what would cause the horseshoe-like vortices to shed from opposite sides of the sample as it was falling. This is clearly depicted in Figures 37a and 37b for the damped case and Figures 40a, 40b, and 40c for the undamped case.

The second observation that was a slight rotation that was noticed of the plane of translational motion of the disks [15]. This same rotational motion was seen in some of the DYE series samples and some of the samples used for timed experiments when viewed from above. Willmarth does not state a number of times that this rotation occurred during a given run, but said that it was slight [15]. Some of the samples of fiberglass would rotate several times before reaching the bottom of the column. This rotation would cause changes to the regularity of the vortices that were being shed in the wake of the clusters. During settling experiments, it was noted that the cause of the rotation of the samples was sometimes attributed to the cluster having a "tail", that is a smaller section of fiberglass that was connected to the larger body of the sample. This "tail" would cause the sample to fall in a spiral pattern, and would also orient the sample such that the full projected area was not perpendicular to the fall direction.

In conclusion for the dye testing, the wake behavior is similar to the observations by Willmarth et al. The vortices that are formed look similar, and the oscillations occur at similar Reynolds numbers and with the same translational motion. They differ in the motion of thin disks because of the shape irregularities and randomness that are inherent of the fiberglass clusters. The wakes look similar, but will change for one sample of fiberglass through a fall distance of 130 cm, whereas the dye trails form disks would be almost identical for the same disk throughout its entire fall distance. This can be seen more so at higher Reynolds numbers (above 100) and in the comparison of Figure 41b to 44a and 44b. The dye trails of the disks form almost circular vortices, while for the clusters there isn't always a distinct shape.

Without a way to accurately measure the moment of inertia for a cluster, a direct stability comparison is not possible, however the all of the cluster samples above a Reynolds number of 100 were unstable, while the samples below it were stable with the exception of DYE 06. This last sample was sufficiently large with a characteristic length equal to 11.88mm, this is one of the larger characteristic lengths that was tested in this research. The sample was also sufficiently thick, and if it is assumed that this sample has a large dimensionless moment of inertia then the oscillatory motion of all of the dye tested samples matches the motion seen by Willmarth et al [15].

Validation of an assumption made in chapter three was also achieved through the DYE series of tests. In order to calculate the stagnation pressure on the face of a particle we have to assume there is little or no flow through the particle. This assumption is key for the calculation of the measured drag coefficient. From all the images portrayed in Figures 36a through 41c, there is no visual evidence of flow through the porous cluster. This confirms that assumption was a valid one, and that the calculations of flow through the particle were accurate.

Chapter 6 Conclusions

The idea behind the experiments run for this research was to find a way to predict the settling velocity of an individual fiber cluster based on the size properties of that cluster. Through three series of tests, sufficient data has been collected to validate an existing correlation to do just that. The correlation developed by Cheng based on historic data of the fall velocity of sand grains can be used directly on fibrous Nukon particles when several assumptions are made. The first is that the fiberglass retains its as fabricated porosity, and the second is that there is no flow through the particles themselves.

Originally, it was thought that the values used in the Cheng correlation for the constants A_*, B, and n were going to have to be modified to fit the new data. After experimentation, however it was found that the Cheng correlation predicts the drag coefficient for fiber clusters quite nicely. From Figure 28 it can be seen that the fiber cluster data follows the trend set by the Cheng correlation [4] quite nicely. There does however, seem to be some bias when the different preparation methods are looked at individually.

The smaller clusters that are formed during the post processing procedure differ in shape and density to clusters that are not post processed. This violates one of the assumptions needed for accurate drag coefficient measurements. This can be accounted for if the CSF [9] is used along with projected are and perimeter measurements when categorizing a particular batch of fiber. Post processed fiber had significantly higher values for the CSF when compared with unprocessed fiber. It is noted that the Cheng correlation over predicts the drag coefficient for clusters with CSF above 0.3. If this fact is taken into consideration when using the Chen correlation to predict the drag, and then subsequently predict the settling velocity of particles, then the correlation remains valid.

The second assumption that must be valid in order to use the data collected in this research was further verified through flow visualization. The particles of fiberglass that are the focus of this research

are porous in nature. Dye testing revealed that there was in fact no flow penetrating the particles. The flow visualization experiments also lead to interesting comparisons to the free settling of thin disks. Behaviors of the wakes of the fiber clusters were similar to the behavior of the wakes of thin disks at similar Reynolds numbers. The wakes formed by the disks are more regular and the vortices are better formed than that of the fiber clusters, but that is to be expected when comparing the symmetry of a disk to the irregularity of a fiber cluster.

The quantitative and qualitative results collected for this thesis lead to the following conclusion. It is possible to model prepared NUKON fiberglass clusters as amorphous thin disks of uniform thickness. The measurement methods provided by these experiments provide a way to calculate a characteristic length for fiber clusters that can be used within the Cheng correlation to predict the drag coefficient, and subsequently the velocity for a single cluster.

Settling is the simplest form of transport that a cluster can be under. Now that measuring techniques are in place, and fiber clusters can be approximated as disks, future work would include extending the principles learned in settling to entrained cluster transport, and ultimately to tumbling transport. Future work would involve placing samples in known flow conditions and timing the fall velocity as well as the distance it takes for the clusters to reach a specified height. Utilizing the same measuring techniques for entrained transport tests could potentially uncover if the clusters behave in a way such that still water settling can be superimposed with bulk fluid motion.

References

[1] "Potential Impact of Debris Blockage on Emergency Recirculation During Design Basis Accidents at Pressurized-Water Reactors," Nuclear Regulatory Commission Generic Letter 2004-02, September 2004

[2] Kryk, H., Hoffmann, W., Waas, U., "Influence of corrosion processes on the head loss across ECCS sump strainer" *Kerntechnik, Vol. 76, No. 1, 2011, pp. 46-53*

[3] Ali, A. F., and Blandford, E. D., "Conventional and Chemical Head Loss Modeling of Multi-Constituent Debris Beds in Resolution of GSI-191," *Proceedings of the Sixteenth International Topical Meeting on Nuclear Reactor Thermalhydraulics,* American Nuclear Society, Chicago, Illinois, 2015,

[4] Ali, A. F., and Blandford, E. D., "An Experimental Study on Head Loss of Prototypical Fibrous Debris Beds During Loss of Coolant Accident Condtions," *ASME Journal of Nuclear Engineering and Radiation Science, Vol. 2, No. 3, 2016*

[5] Lee, S., Brockmeyer, L. M., Sulaiman, S. A. B., and Hassan, Y. A., "Temperature Effect on Small Size NUKON Fibrous Debris Settling Velocity," *Transactions of the American Nuclear Society, Washington, D.C., 2013*

[6] Maji, A. K., Rao, D. V., Letellier, B., Bartlein, L., and Marshall, B., "Transport Characteristics of Selected Pressurized Water Reactor LOCA-Generated Debris," *Nuclear Technology, Vol. 139, No. 2, 2002, pp. 145-155*

[7] Zigler, G., Rao, D. V., Shaffer, C., Souto, F., and Thomas, W., "Parametric Study of the Potential for BWR ECCS Strainer Blockage Due to LOCA Generated Debris," NUREG/CR-6224, Science and Engineering Associates Inc., Albuquerque, NM, October 1995

[8] "ZOI Fibrous Debris Preparation: Processing, Storage and Handling," Nuclear Energy Institute, January 2012

[9] Corey, A. T., "Influence of Shape on the Fall Velocity of Sand Grains," *Colorado State University Masters Thesis, 1949*

[10] Komar, P. D., and Reimers, C. E., "Grain Shape Effects on Settling Rates," *The Journal of Geology, Vol. 86, No. 2, 1978, pp. 193-209*

[11] Souto, F. J., and Rao, D. V., "Experimental Investigation of Sedimentation of LOCA-Generated Fibrous Debris and Sludge in BWR Suppression Pools," NUREG/CR-6368, Science and Engineering Associates Inc., Albuquerque, NM, December 1995

[12] Rao, D. V., Letellier, B. C., Maji, A. K., and Marshall, B., "GSI-191: Separate-Effects Characterization of Debris Transport in Water," NUREG/CR-6772, Los Alamos National Laboratory, Los Alamos, NM, August 2002

[13] Cheng, N. S., "A Simplified Settling Velocity Formula for Sediment Particle," *ASCE Journal of Hydraulic Engineering, Vol. 123, No. 2, 1997, pp. 149-152*

[14] Camenen, B., "Simple and General Formula for the Settling Velocity of Particles," *ASCE Journal of Hydraulic Engineering, Vol. 133, No. 2, 2007, pp. 229-233*

[15] Willmarth, W. W., Hawk, N. E., and Harvey, R. L., "Steady and Unsteady motions and Wakes of Freely Falling Disks," *The physics of Fluids, Vol. 7, No. 2, 1964, pp. 197-208*

[16] Kim, A. S., and Stolzenbach, K. D., "The Permeability of Synthetic Fractal Aggregates with Realistic Three-Dimensional Structure," *Journal of Colloid and Interface Science, Vol. 253, 2002, pp. 315-328*